

JGR Atmospheres

RESEARCH ARTICLE

10.1029/2021JD035772

Key Points:

- Trans-Himalaya long-range transport is evident with significant black carbon (BC) transport flux aloft above Himalayas and Tibetan Plateau and free troposphere from South Asia (SA) and East Asia (EA) region
- Synergy on aerosol-boundary feedback interaction manifested that BC expand planetary boundary layer height by 5.01% and 4.80% over SA and EA, respectively
- Elevated BC caused notable warming over Tibetan Plateau that could pose a threat in the cryosphere over that region

Supporting Information:

Supporting Information may be found in the online version of this article.

Correspondence to:

J. Yang,
yangjunhua@lzb.ac.cn

Citation:

Rai, M., Kang, S., Yang, J., Chen, X., Hu, Y., & Rupakheti, D. (2022). Tracing atmospheric anthropogenic black carbon and its potential radiative response over Pan-Third Pole region: A synoptic-scale analysis using WRF-Chem. *Journal of Geophysical Research: Atmospheres*, 127, e2021JD035772. <https://doi.org/10.1029/2021JD035772>

Received 14 SEP 2021

Accepted 11 FEB 2022

Author Contributions:

Conceptualization: Mukesh Rai, Shichang Kang

Data curation: Mukesh Rai, Junhua Yang

Formal analysis: Mukesh Rai

Funding acquisition: Shichang Kang

Investigation: Mukesh Rai, Xintong Chen

Methodology: Mukesh Rai, Junhua Yang

Project Administration: Shichang Kang





Resources: Shichang Kang

Software: Mukesh Rai

Supervision: Shichang Kang, Junhua Yang

Validation: Mukesh Rai

Tracing Atmospheric Anthropogenic Black Carbon and Its Potential Radiative Response Over Pan-Third Pole Region: A Synoptic-Scale Analysis Using WRF-Chem

Mukesh Rai^{1,2} , Shichang Kang^{1,2} , Junhua Yang¹ , Xintong Chen^{1,2}, Yuling Hu¹, and Dipesh Rupakheti³ 

¹State Key Laboratory of Cryospheric Science, Northwest Institute of Eco-Environment and Resources, Chinese Academy of Sciences, Lanzhou, China, ²University of Chinese Academy of Sciences, Beijing, China, ³Jiangsu Key Laboratory of Atmospheric Environment Monitoring and Pollution Control, Collaborative Innovation Center of Atmospheric Environment and Equipment Technology, School of Environmental Science and Engineering, Nanjing University of Information Science & Technology, Nanjing, China

Abstract The Pan-Third Pole contains the largest number of glaciers outside the polar region that plays a crucial role in atmospheric circulation and the hydrological cycle. However, this pristine region has undergone rapid change through complex interactions including the black carbon (BC) enhanced warming effect and glacier melting. Study shows, Weather Research and Forecasting coupled with Chemistry (WRF-Chem) simulation is able to capture distinctive seasonal variability of BC. The result from our sensitivity experiments revealed that South Asia (SA; 60.7%) and East Asia (EA; 32.9%) contributed more toward the Tibetan Plateau (TP). Our analysis on aerosol-boundary feedback interaction revealed BC expand planetary boundary layer height by 5.0% and 4.8% over SA and EA, respectively, which facilitates BC dispersion and transportation. Whereas, we also found that under the influence of different wind regimes the significant BC transport flux aloft over the TP and the upper troposphere and lower stratosphere. Additionally, mountain-valley channel and synoptic and local meteorological processes also facilitated BC transport to the TP. This study also evaluated the effect of BC on direct radiative forcing and calculated subsequent temperature changes. A strong dimming effect of BC corroborated with the following negative surface temperature changes. However, enhanced BC concentration during winter and spring caused the increase in temperature over the TP. Here, the WRF-Chem model, synergy on aerosol-boundary feedback, BC transport flux, and source-receptor methods confirmed the significant BC contribution and transportation, and notable BC-induced warming over TP. Such trans-Himalayan BC transport and associated warming could grim glacier melt and water availability in the region.

1. Introduction

The Pan-Third Pole (PTP) region is home to 3 billion people that provides ecological and cryospheric services and plays a crucial role in the global climate system (Bolch et al., 2012; Immerzeel et al., 2010; Jin et al., 2005; Kang et al., 2019; Viviroli et al., 2007; Yao et al., 2019; Yuan et al., 2018). However, the growing body of evidence suggests this relatively pristine region has undergone a rapid change in recent years (Chen et al., 2013; Kang et al., 2010; Yao et al., 2019). Previous meteorological records (Huang & Ma, 2016; You et al., 2013), reanalysis data sets (Frauenfeld et al., 2005), modeling works (Ma et al., 2017; Zhu et al., 2013), and elevation-dependent warming studies (Du et al., 2019; You et al., 2020) have manifested unprecedented warming over the PTP that is highly stressed out in this climatically sensitive region. Atmospheric brown cloud is considered as a potent agent that further amplify the warming trend in Asia (Bonasoni et al., 2010; Nakajima et al., 2007; Ramanathan & Carmichael, 2008), which is mainly composed of black carbon (BC). BC has been argued as the second strongest anthropogenic source of global warming and climate change next to CO₂ (Bond et al., 2013; Gustafsson & Ramanathan, 2016; Hansen et al., 2000; Jacobson, 2001). As noted by Xu et al. (2016), the BC-induced warming rate over the Himalayas and Tibetan Plateau (HTP) is twice the global average. Moreover, it is well-known that the depositional BC on snow and glacier surface melt can be accelerated through an albedo feedback mechanism (Flanner et al., 2009; Ji, 2016; Kang et al., 2019, 2020; Ming et al., 2008; Wiscombe & Grams, 1976).

Asia's two biggest growing economies countries, China and India, are contributing high emissions of anthropogenic aerosols to the atmosphere in recent decades, deteriorating environmental air quality, and threatening human health (Davidson et al., 2005; Kang et al., 2019; Ravishankara et al., 2020). Despite being located remotely,

Visualization: Mukesh Rai

Writing – original draft: Mukesh Rai, Shichang Kang, Junhua Yang, Xintong Chen, Yuling Hu, Dipesh Rupakheti

Writing – review & editing: Mukesh Rai, Shichang Kang, Junhua Yang, Xintong Chen, Yuling Hu, Dipesh Rupakheti

the BC concentrations in the Tibetan Plateau (TP) are notable that could be facilitated by long-range transport from neighboring regions (Chen et al., 2018; Kaspari et al., 2014; Kopacz et al., 2011; Lüthi et al., 2015; Ming et al., 2008). According to Zhang et al. (2015) and Zhao et al. (2021), the local anthropogenic BC emission from the TP holds a small proportion in comparison with external influences. Thus, it is worthy to explore more about non-local BC contribution and transport mechanism over the TP. So far, different modeling approaches such as tracer-tagging (Kumar et al., 2015; Zhang et al., 2015), adjoint (Kopacz et al., 2011), backward-trajectory (Lu et al., 2012; Lüthi et al., 2015), and emission perturbation (Han et al., 2020; Yang et al., 2018) have been used to simulate source and transportation of BC over the TP. As noted by Zhang et al. (2015) and Han et al. (2020), the backward-trajectory method performed well on source regions close to the receptor on a short timescale, but this approach has limitations in determining contributions of BC to receptor far from source in the middle and upper troposphere. Similarly, the adjoint method provides a global distribution of emission that directly contributes to BC concentration at receptor locations, thus, results are not sourced attribution but the source-receptor sensitivity (Zhang et al., 2015). In this study, we applied an emission perturbation approach followed by Han et al. (2020) and Yang et al. (2018). This method enables to estimate BC contributions from source to receptor region by turning off BC emissions from particular source region.

To our knowledge, most of the previous studies are focused in Central Asia (CA), South Asia (SA), and North-East China (Kulkarni et al., 2015; Kumar et al., 2015; Sarangi et al., 2019; Yang et al., 2018; Zhang et al., 2017; Zhang, Chen et al., 2020; Zhao et al., 2013). However, it remains unclear about the underlying mechanism involved in a complex interplay of aerosol-boundary layer interaction, vertical and horizontal BC transport flux, and BC transportation to the TP from the PTP subregion and radiative perturbation. Owing to its unique geographic location (complex highland bounded by two major polluted countries), the PTP makes an ideal place to study the contribution, transport mechanism, and associated radiative impact of BC. Over this region, the role of BC has been a topic of high interest from the atmosphere-cryosphere point of view. However, inadequate representation of long-term BC observation data over the region is further deemed by harsh environmental conditions. Therefore, to overcome such disparity, the modeling framework could be an asset for extending the current understanding for the quantitative assessment of BC contribution and transport mechanism to TP and associate discernible role on climate. To assess this, we trained and deployed the Weather Research and Forecasting coupled with Chemistry (WRF-Chem) model. The rest of the paper follows the model description and set up in Section 2, the result and discussion in Section 3, and the conclusion in Section 4.

2. Methods

2.1. WRF-Chem Model

In this study, the state-of-the-art mesoscale community model (Skamarock et al., 2005) coupled with the chemistry module WRF-Chem (version 3.6; Grell et al., 2005) was used to investigate the spatio-temporal variation, contribution, transportation, and radiative perturbation of BC over the PTP for the year 2017. This Eulerian chemical transport model enables to process emission, advection, deposition, chemical transformation of aqueous and gaseous, and aerosol chemistry and dynamics (Grell et al., 2005). An aerosol chemistry module, Goddard Chemistry Aerosol Radiation Transport (GOCART; Ginoux et al., 2001) is embedded with the Model for Simulating Aerosol Interactions and Chemistry (MOSAIC) aerosol model (Zaveri et al., 2008) within the WRF-Chem framework by Zhao et al. (2010). The GOCART produces output for seven bulk aerosol species that include BC (BC1, BC2), organic carbon (OC1, OC2), particulate matter (PM_{2.5}, PM₁₀), and sulphate. Spherical shape and major aerosol species (i.e., BC, OC, SO₄²⁻, NO₃⁻, NH₄⁺, sea salt, and mineral dust) were considered within the model framework. The Carbon Bond Mechanism (CBMZ; Zaveri & Peters, 1999) was implemented into WRF-Chem by Fast et al. (2006), which offers the complex treatments of aerosol radiative properties and photolysis rates. This model has been widely used for the assessment and prediction of air quality, weather forecast, atmosphere-cryospheric interaction, and aerosol interaction with radiation and atmosphere (Ding et al., 2019; Feng et al., 2016; Kumar et al., 2015; Ukhov et al., 2020). Particularly, over complex terrain, the performance of the WRF-Chem model is known to have large uncertainty. However, previous studies carried out on such terrain for the systematic evaluation with fine resolution of the model were found to reproduce within acceptable bias range (Karki et al., 2017; Mues et al., 2018; Norris et al., 2020; Sarangi et al., 2019; Zhang, Zhao, et al., 2020).

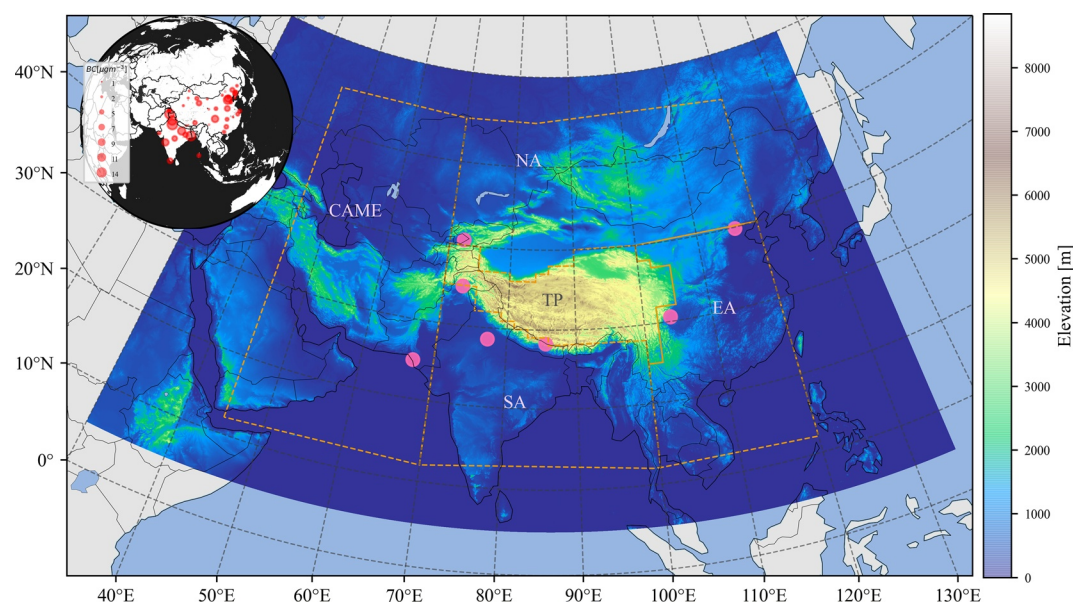


Figure 1. Sketch map for the Pan-Third Pole region terrain and its surrounding areas. The magenta circular dots represents meteorological stations. The red dot (size represents concentrations) in the upper left corner shows measured black carbon (BC) concentration during the simulation period. The yellow dashed line distinguishes identical subregions.

2.2. Model Set up and Experiment Design

WRF-Chem domain was configured covering the PTP region (as shown in Figure 1) at 30-km horizontal resolution with grid cell spacing 150×208 (45°E – 120°E , 05°N – 55°N). The domain centered at 35°N , 82°E , and stretched up to 40 vertical sigma levels from the surface to the top of the level (50 hPa). Initial meteorological fields and lateral boundary conditions were fed from the National Center for Environmental Prediction final analysis (NCEP/FNL) data archived at 1° horizontal resolution, which provided every 6-hr temporal intervals. The initial and boundary conditions of aerosol-chemistry were calculated using mozbc utility tool based on the output of Model for Ozone and Related Chemical Tracers (MOZART; Emmons et al., 2010). The simulation run period started from 1st January–31st December 2017, where the early week of January was allowed to model spin-up. The physical parameters were chosen based on the previous work by Yang et al. (2018) and You et al. (2012) where they proved the model's ability to reproduce well under consideration of such parameterization over the TP region. As summarized in Table 1, the following detailed parameterization modules were included in our modeling framework.

The revised MM5 (Paulson, 1970) and unified Noah (Chen & Dudhia, 2001; Ek et al., 2003) schemes are chosen to represent the surface and land interactions. The Rapid Radiative Transfer Model (RRTMG) for both shortwave and longwave is used for the aerosol direct radiative effects (Iacono et al., 2008; Mlawer et al., 1997). The Morrison-2-moment is used for the treatment of the microphysics process (Gustafson et al., 2007). The Yonsei University (YSU) scheme was selected to describe the planetary boundary layer, whereas Grell 3D ensemble scheme (Grell et al., 1994) reproduces cloud and precipitation processes.

To understand the contribution and climate response to the direct effect of BC, we designed five sets of experiments. It should be noted that the direct effect of BC as climatic response and contribution from surrounding to the TP presented here is the difference between the control experiment and the associated sensitive experiment, which are zonally averaged. One control and five sensitive experiments were carried out to investigate anthropogenic BC impacts from the subregional level to the TP. In five sensitive experiments, anthropogenic BC emission flux was turned off (set as zero) while it was included in the control experiment. The details of the experimental design

Table 1
Key Parameterization Schemes Adopted in the WRF-Chem Simulation

Parameterization	Scheme
Surface layer	Revised MM5
Land surface	Unified Noah
Radiative transfer (SW)	RRTMG
Radiative transfer (LW)	RRTMG
Boundary layer	Yonsei University (YSU)
Cumulus option	Grell 3D
Microphysics	Morrison 2-moment
Dust emissions	GOCART
Aerosol chemistry	GOCART/RACM

Note. RACM, Regional Atmospheric Chemistry Mechanism; RRTMG, Rapid Radiative Transfer Model; GOCART, Goddard Chemistry Aerosol Radiation Transport.

Table 2
Experimental Setup

Case	Description
Control	Anthropogenic black carbon (BC) included throughout the entire domain
All_noBC	Anthropogenic BC not included throughout the entire domain
CAME	BC set to zero for Central Asia and Middle East “CAME” domain
SA	BC set to zero for South Asia “SA” domain
EA	BC set to zero for East Asia “EA” domain
NA	BC set to zero for North Asia “NA” domain

are given in Table 2. Further, to assess the contribution and radiative impact of BC, the difference between control and sensitivity experiments was evaluated on a seasonal basis. Additionally, we have used a control and sensitivity experiment (All_noBC) to understand the synergetic effect of aerosol-boundary layer interaction. The BC-induced planetary boundary layer height (PBLH) changes are the difference between control and sensitivity experiments.

2.3. HYSPLIT Model

To provide evidence for the long-range transport of BC, the Hybrid Single-Particle Lagrangian Integrated Trajectory (HYSPLIT) model was initialized at 100-m above sea level for the 6-hr interval (UTC, 00:00, 06:00, 12:00, and 18:00). Considering atmospheric BC's life span of about 7 days, the model was forced to run for 168 hr using the Global Data Assimilation System (GDAS, 1° spatial resolution) gridded meteorological reanalysis data set for backward trajectories generation for the year 2017. The potential source contribution function (PSCF) was used for the computation of the potential source contribution factor based on BC observation data from the Qomolongma station for Environmental Observational and Research (QOMS, 28.36°N, 86.95°E, 4,275 m a.s.l.) site which is located on the northern slope of Mt. Everest. To avoid the possible uncertainty, rain-bearing trajectories were sorted out (Cross, 2015). Here, we used a Gaussian filter and continuous weighting function to smooth out the results.

$$WF_{ij} = \frac{\log(N_{ij})}{\log(\max(N))}$$

where, WF_{ij} = weighted function for N_{ij} trajectories and N = total number of trajectories.

2.4. Emission, Meteorological Observation, and Reanalysis Data Set

The gridded anthropogenic emissions data set was taken from the updated emissions inventory Emission Database for Global Atmospheric Research and Hemisphere Transport of Air Pollution (EDGAR-HTAP, v2.2; Janssens-Maenhout et al., 2015). EDGAR-HTAP emission data set has been compiled using regional emissions grid maps for BC, OC, $PM_{2.5}$, PM_{10} , CO, CH_4 , SO_2 , NO_x , NH_3 , and non-methane volatile organic compounds (NMVOC), which further reports monthly emission data from different emission sectors like residential, industry, power, agriculture, ground transport, aviation, and shipping at a $0.1^\circ \times 0.1^\circ$ spatial resolution. For Asia, emission inventory data from the Emissions Database for Global Atmospheric Research (EDGAR, v4.3) was used to fill the data gap in the Model Inter-comparison Study for Asia (MICS-Asia III). It should be noted that, due to incomplete reporting and large uncertainties of land-use and forest-related biomass burning emissions, EDGAR-HTAP does not deliver these emissions thus, as suggested by Janssens-Maenhout et al. (2012) we used the data set from fire emission inventory NCAR (FINN, v1; Wiedinmyer et al., 2011). The biogenic emissions data set was derived from the Model of Emission of Gases and Aerosol from Nature (MEGAN; Guenther et al., 2006).

The daily average meteorological parameters such as temperature, relative humidity (RH), and wind speed were obtained from the weather underground portal (<https://www.wunderground.com/>). As shown in Figure 2, the parameters were retrieved for Beijing (39.86°N, 116.28°E), Chengdu (30.58°N, 103.92°E), New-Delhi (28.59°N,

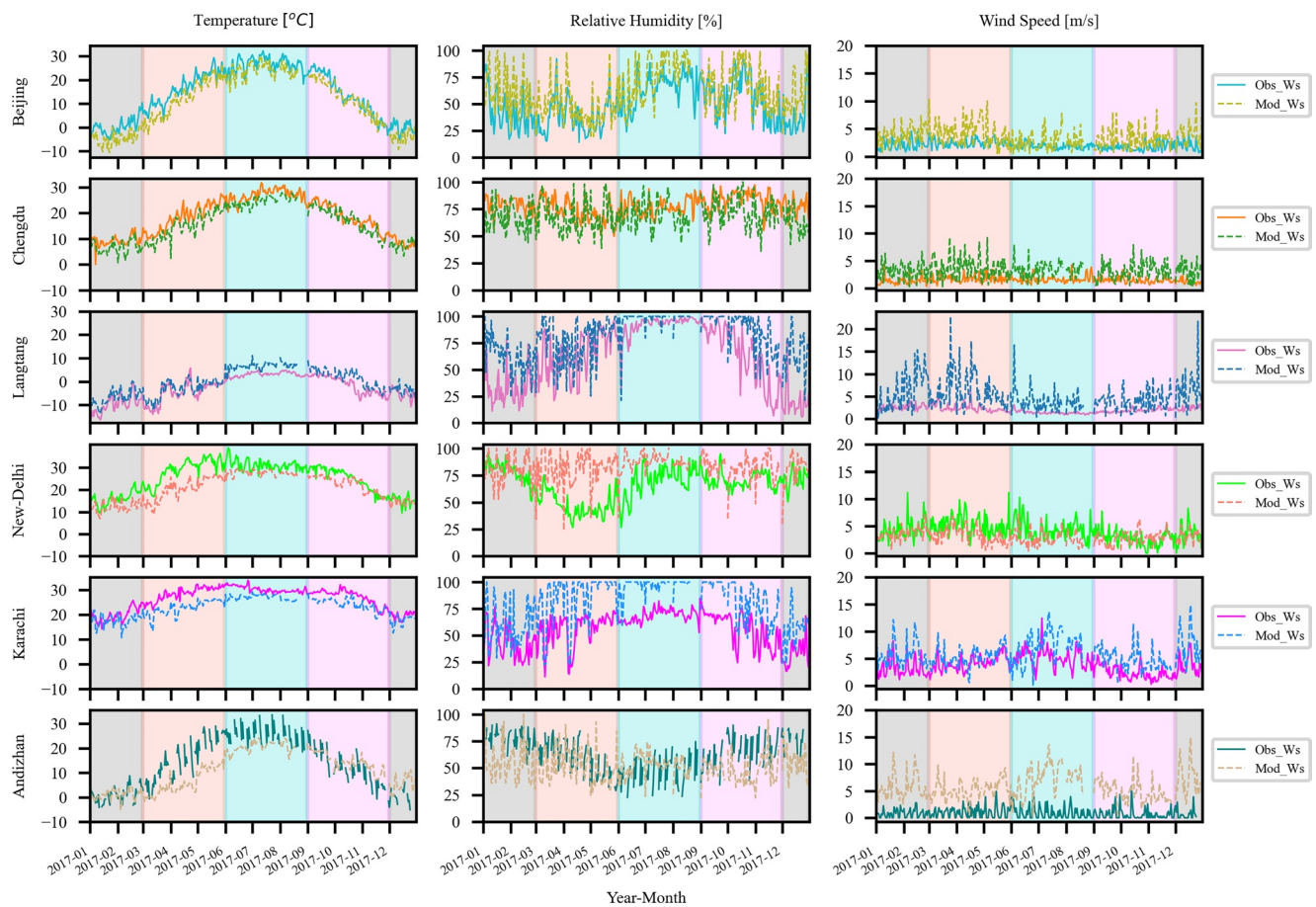


Figure 2. Time series of observed and simulated temperature, relative humidity, and wind speed for the year 2017. For identical stations, the solid and dashed lines represents observations and simulation data, respectively. From left to right, different bar colors respectively shows the winter, spring, summer, and autumn seasons.

77.26°E), Karachi (24.87°N, 67.11°E), and Andizhan (40.66°N, 72.26°E) whereas for Langtang (28.23°N, 85.61°E), the data were obtained from a regional database system (ICIMOD, 2016).

Here, we examined the spatial variation of temperature, precipitation, and wind for the whole domain by asserting the climate reanalysis data set. The gridded near-surface temperature was obtained from Climate Research Unit (CRU, <http://www.cru.uea.ac.uk/data>). Other than this, we used the fifth generation of the European Centre for Medium-Range Weather Forecasts (ECMWF-ERA5) atmospheric reanalysis products for the assessment of wind profile and temperature. ERA5 reanalysis products (gridded at $0.25^\circ \times 0.25^\circ$) are derived applying bias and sequential elevation correction methods (Cucchi et al., 2020; Weedon et al., 2014). In addition to this, we also used wind data from National Centers for Environmental Predictions (NCEP) reanalysis (<https://psl.noaa.gov/data/>). We retrieved temperature and precipitation (at surface level) and wind (at 500 hPa) from Copernicus Climate Change Service (C3S, <https://cds.climate.copernicus.eu>). The daily-accumulated precipitation product, Tropical Rainfall Measuring Mission (TRMM) was generated from three hourly TRMM Multi-Satellite Precipitation Analysis TMPA (3B42). We extracted TRMM data product (Level-3, version-7) from Goddard Earth Sciences Data and Information Services Center (GES DISC, <https://disc.gsfc.nasa.gov/>) which has a spatial resolution of $0.25^\circ \times 0.25^\circ$.

2.5. BC Transport Flux Calculation

The horizontal and vertical transport of pollutants accumulation and dispersion depend on different meteorological fields, of which wind regime plays a crucial role. A similar approach of calculation of sensible heat (Stull, 1988), BC transport flux can be calculated by relating the fluctuation between wind field and BC mass

Table 3

Comparison of Statistical Score Summary of Meteorological Parameters in Observation Sites With Model Output

Sites	Temperature				Relative humidity				Wind speed			
	RMSE	MB	R	SD	RMSE	MB	R	SD	RMSE	MB	R	SD
Beijing	4.21	3.49	0.98	11.47	4.21	-10.75	0.71	22.03	2.36	-1.55	0.42	1.96
Chengdu	3.56	2.50	0.94	7.32	17.61	9.42	0.18	13.20	2.48	-1.81	0.54	1.61
Langtang	3.47	-2.68	0.92	5.59	30.28	-20.30	0.64	20.82	4.47	-2.97	0.24	3.44
New Delhi	5.64	4.33	0.86	6.13	25.07	-17.15	0.15	12.34	2.21	1.00	0.32	1.34
Karachi	4.44	3.66	0.85	4.05	30.28	-25.87	0.71	22.37	3.07	-2.09	0.50	2.48
Andizhan	7.34	3.06	0.78	7.83	24.35	9.91	0.32	14.01	2.37	-1.59	0.28	1.50

Note. RMSE, root mean square error; MB, mean bias; SD, standard deviation.

concentrations from surface to different layer of atmosphere. Here, we have calculated BC transport flux using a similar approach used by Yuan et al. (2019) and Joshi et al. (2021). The BC transport flux (TF_{bc}) can be obtained as follows:

$$TF_{bc} = BC_i \times w_i$$

where BC_i and w_i represent the BC mass concentrations and wind components in each model layer.

2.6. Model Evaluation Metrics

We examined the skill of model performance utilizing observation and reanalysis data set against model output. Point-based propagation was assessed for the meteorological parameters (temperature, RH, and wind speed). Meteorological parameters play an important role in air quality; therefore, we focused on the evaluation of these parameters using in-situ observation and reanalysis data sets. In addition, to examine distribution patterns at the synoptic scale, we used near-surface and reanalysis data sets for temperature, wind, and precipitation. The statistical metrics used to assess the model performance are root mean square error (RMSE; Equation 1), mean bias (MB; Equation 2), and Pearson correlation coefficient (R; Equation 3).

$$RMSE = \sqrt{\frac{\sum_{i=1}^N (M_i - O_i)^2}{N}} \quad (1)$$

$$MB = \frac{1}{N} \sum_{i=1}^N (M_i - O_i) \quad (2)$$

$$R = \frac{1}{N-1} \sum_{i=1}^N \left(\frac{M_i - m}{\sigma_M} \right) \left(\frac{O_i - o}{\sigma_o} \right) \quad (3)$$

Here, the metrics calculated, with N , M_i , O_i , m , o , σ_M , and σ_o are the number of observation and model data, model value, observed value, model mean, observed mean, and standard deviation model/observed, respectively.

3. Results and Discussion

3.1. Meteorology

The comparison of simulated annual mean temperature, RH, and wind speed with concurrent observed data for the selected stations is listed in Table 3. For all stations, the temperature was reproduced well by the model ($R = 0.78-0.98$) compared to its performance on RH and wind speed. A yearlong temperature MB exhibited positive bias in five locations except for Langtang where cold bias ($MB = -2.68$) was found. Although, RH underestimation in Beijing ($MB = -10.75$), Langtang ($MB = -20.30$), Karachi ($MB = -25.87$), and New Delhi ($MB = -17.15$), relatively good correlation values of 0.71, 0.64, and 0.71 were found in sites. The wind speed has an essential impact on pollution transport with low speeds favoring the accumulation of pollutants in source proximity, whereas higher speeds lead to pollution dispersion. The wind speed over all the stations was under-

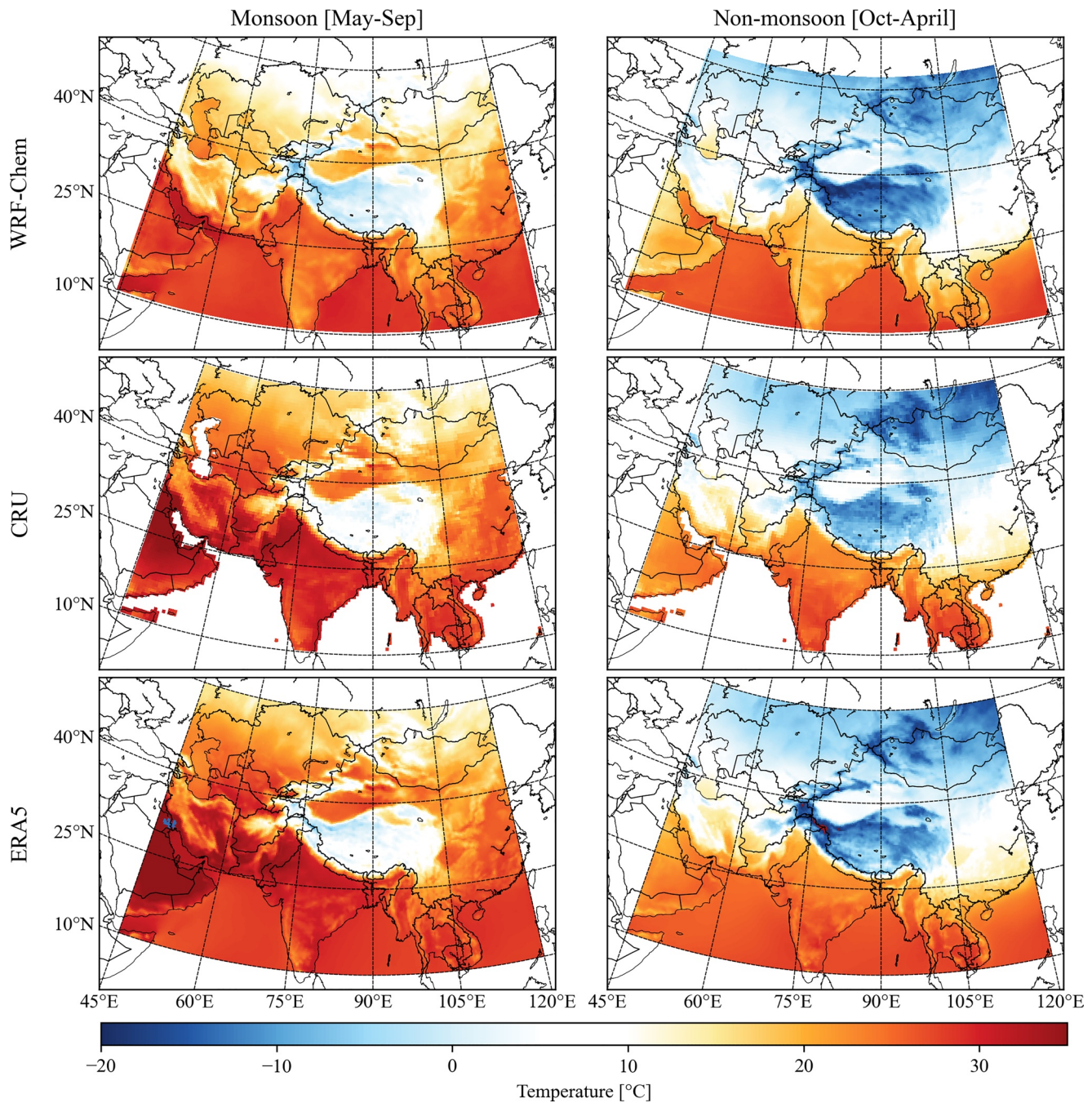


Figure 3. Spatial distribution of mean surface air temperature from Weather Research and Forecasting coupled with Chemistry (WRF-Chem), Climate Research Unit (CRU), and ERA5 for monsoon and non-monsoon seasons.

estimated with MB up to -2.97 m s^{-1} . The RMSE values of Beijing (2.36 m s^{-1}), Chengdu (2.48 m s^{-1}), New Delhi (2.21 m s^{-1}), and Andizhan (2.37 m s^{-1}) are close to the benchmark value of 2 m s^{-1} as proposed by Emery et al. (2001) whereas, in the case of Langtang, MB, RMSE, and standard deviation (SD) are twice as higher than other locations. We also compared model results with reanalysis data sets such as temperature (Figure 3), precipitation (Figure 4), and wind field (Figure 5). Zonally averaged statistical metrics in Table 4 and Figure S1 in Supporting Information S1 indicated that temperature reproduced better than precipitation which is further proved statistically. Strong correlation coefficient ($R_m = \text{monsoon}$, $R_{nm} = \text{non-monsoon}$) for temperature were found with WRF-CRU ($R_m = 0.82$, $R_{nm} = 0.96$) and WRF-ERA5 ($R_m = 0.90$, $R_{nm} = 0.93$) than precipitation

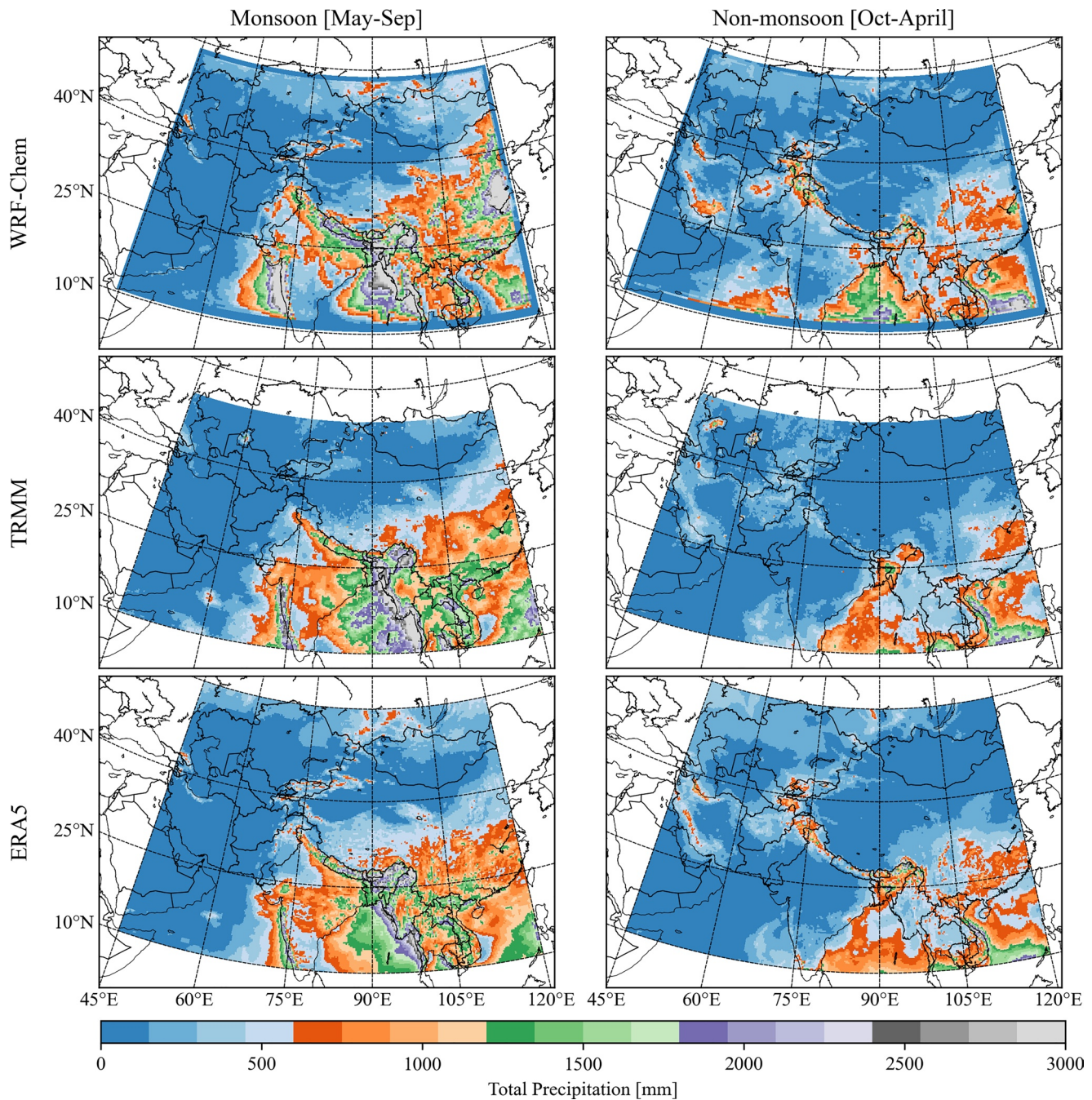


Figure 4. Spatial distribution of total precipitation between monsoon and non-monsoon seasons from Weather Research and Forecasting coupled with Chemistry (WRF-Chem), Tropical Rainfall Measuring Mission (TRMM), and ERA5.

WRF-TRMM ($R_m = 0.80$, $R_{nm} = 0.63$) and WRF-ERA5 ($R_m = 0.30$, $R_{nm} = 0.40$). In contrast to temperature, modeled precipitation has relatively high MB than reanalysis data sets.

WRF-Chem captured seasonal wind profile reasonably well with NCEP and ERA5 at 500 hPa (Figure 5). Except for the summer monsoon, a stronger signal of westerly (20–40°N) air masses was found directed toward East China (EC). In the 90–120°E longitudinal section, north prevailing wind directed toward EC at high wind speed that is potentially due to the Siberian high effect. A clear picture of air mass convergent was captured well over Arabian Peninsula (AP) during summer, however, the strong northward air movement from the Bay of Bengal (BOB), cyclonic activities could not be captured well by the model simulation which possibly led by coarser

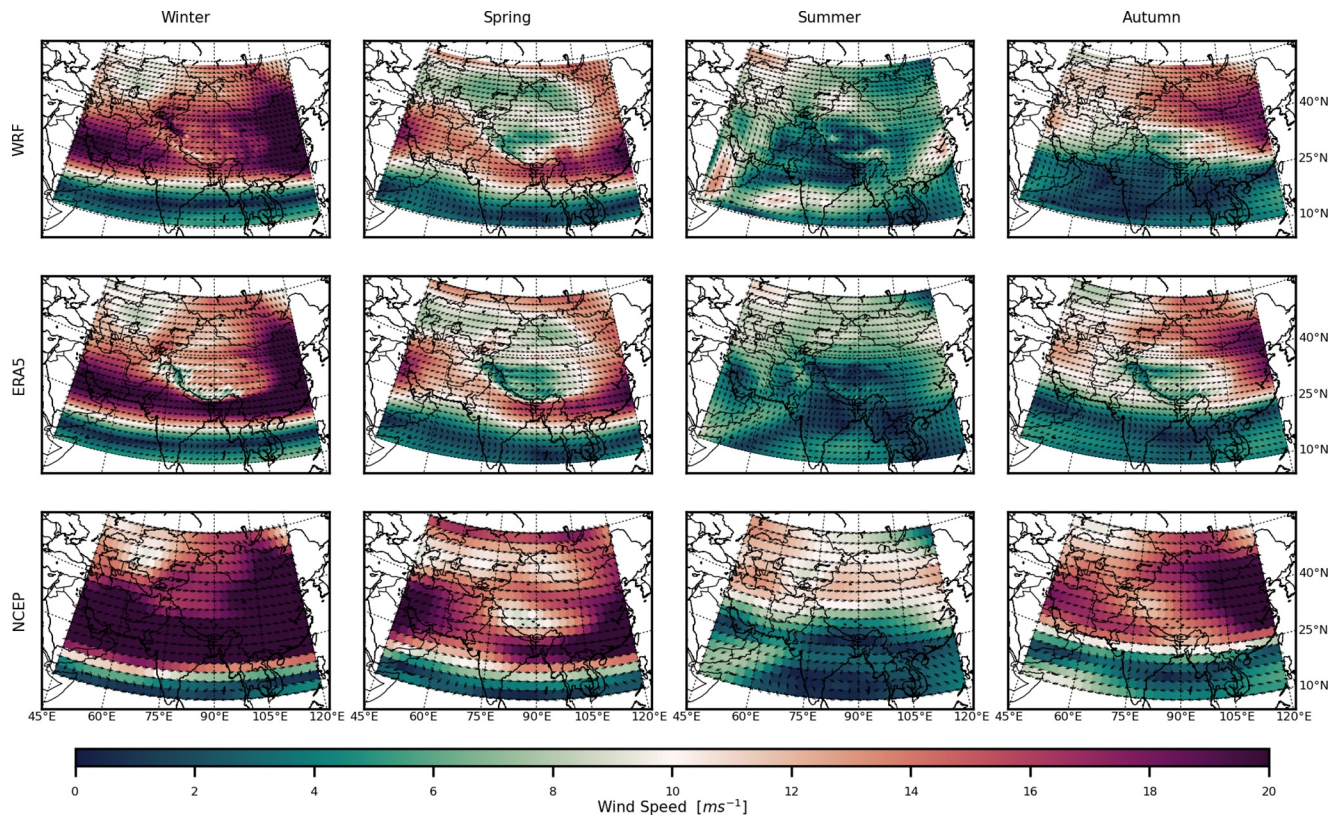


Figure 5. Seasonal variation of wind field (ms^{-1}) at 500 hPa from Weather Research and Forecasting (WRF) simulation, ERA5, and National Center for Environmental Prediction (NCEP) data. The reference vector used in the map is of magnitude 5 m/s. Color-coded data in the background of the figure represents the wind speed.

resolution of the model. At a given pressure height, stronger and weak wind speeds were observed during the winter and summer seasons, respectively. In comparison with WRF-Chem and ERA5, NCEP overestimates the wind speed as this data set has a coarser spatial resolution ($2.5^\circ \times 2.5^\circ$). The zonal average seasonal correlation between model and reanalysis was found in the range of 0.64–0.94 indicating the model's capability to reproduce in an acceptable range. However, inaccurate representation of wind field is predominant over mountainous terrain (Mar et al., 2016; Mues et al., 2018; Zhang et al., 2013, 2016), which could potentially be caused by orographic variation, mesoscale mountain-valley circulation, rapid fluctuation on the diurnal cycle of southerly (upslope) and northerly (downslope) winds (Norris et al., 2020; Ueno et al., 2008; Whiteman, 2000).

Table 4

Zonal Average Statistical Metrics Inter-Comparison Between WRF-Chem, CRU, ERA5, and TRMM for Temperature and Precipitation

Detail		Monsoon				Non-monsoon			
		RMSE _m	MB _m	R _m	SD _m	RMSE _{nm}	MB _{nm}	R _{nm}	SD _m
Temperature	WRF-CRU	4.40	−2.46	0.82	6.25	4.45	1.21	0.96	10.77
	WRF-ERA5	9.43	2.32	0.90	3.09	19.43	12.24	0.93	4.55
Precipitation	WRF-TRMM	276.53	−186.21	0.80	312.25	285.11	−180.20	0.63	208.13
	WRF-ERA5	444.79	307.31	0.30	87.90	248.99	120.87	0.40	47.60

Note. RMSE, root mean square error; MB, mean bias; SD, standard deviation; WRF, Weather Research and Forecasting; CRU, Climate Research Unit; TRMM, Tropical Rainfall Measuring Mission.

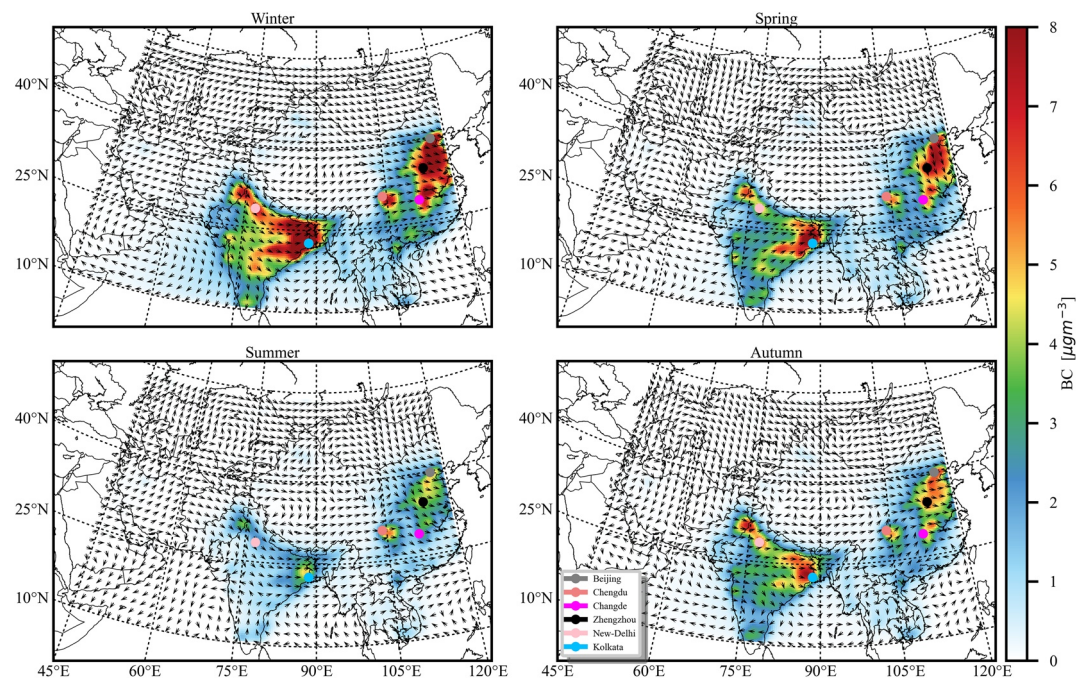


Figure 6. Distribution of simulated seasonal mean surface black carbon (BC) concentrations ($\mu\text{g m}^{-3}$) from the control simulation. The mean horizontal wind (U and V) is plotted at 500 hPa. The different colors represent the identical locations as given in legend.

We have provided more statistical metrics in Figure S6 in Supporting Information S1. Spatial precipitation patterns for monsoon and non-monsoon seasons (Figure 4) indicate that the model reproduced well as compared with TRMM and ERA5. In the left column of Figure 4, the synoptic monsoon was seen active, with maximum total precipitation ($>2,000$ mm) received over parts of Myanmar, Bhutan, Bangladesh, and Nepal. The onset of the monsoon from BOB spreads over the Indo-Gangetic Plain (IGP) region, reaching up to Pakistan in the west and southeast China in the east. In addition, from the Arabian Sea branch, the monsoon arrived mostly in the southern part of India. The gradual withdrawal process removes the precipitation, which can be seen in the right column of Figure 4.

Compared with observation and reanalysis data sets, the simulation biases could be owing to numerous potential reasons such as complex mountain terrain, elevation gradient, lapse rate, moisture processes, overestimation of snowfall, radiative surface heating, as well as cooling feedback (Immerzeel et al., 2014; Kattel et al., 2013). Previous studies indicated that satellite products (Derin & Yilmaz, 2014; Sun et al., 2018) and model simulation (Karki et al., 2017; Mues et al., 2018) have difficulties in reproducing precipitation in areas with complex topography. Precipitation overestimation was reported over SA (Kumar et al., 2012; Rana et al., 2015) and China (Zhao & Yatagai, 2014). Other than local dynamics, overestimation/underestimation could be attributed due to excessive moisture transport flux and precipitation of water from the BOB and the western North Pacific (Raju et al., 2015; Shah & Mishra, 2016).

3.2. Spatio-Temporal Distribution of Surface BC Concentration

Figure 6 shows the spatio-temporal distribution of mean surface BC concentration in the year 2017. In general, the magnitude of simulated BC appeared to be close to the strength of the emission source with higher values in the major polluted region. The higher BC concentrations are identified in and around megacities like Beijing, Chengdu, Changde, Zhengzhou, Dhaka, Kolkata, New Delhi, and Lahore. Whereas, model results show less amount of BC over relatively remote regions of the TP, North Asia (NA), and Central Asia and Middle East (CAME) where anthropogenic influence remains less. In the present study, the anthropogenic BC loading within

Table 5
Comparison of Measured and Simulated Atmospheric BC Concentration ($\mu\text{g m}^{-3}$) at Different Stations During 2017

Sites	Location	Period	Model (Mean \pm SD)	Measured (Mean \pm SD)	Mean ratio
Beijing	39.80°N, 116.47°E	2017	5.866 \pm 4.059	7.350 ^a	1.253
Chengdu	30.65°N, 104.04°E	2017	7.375 \pm 4.098	7.210 ^a	0.978
Changde	29.17°N, 111.71°E	2017	4.115 \pm 2.141	2.340 ^a	0.569
Guilin	25.32°N, 110.30°E	2017	1.984 \pm 0.751	3.140 ^a	1.582
Lhasa	29.67°N, 91.13°E	2017	0.206 \pm 0.117	3.100 ^a	15.038
Lushan	29.57°N, 115.99°E	2017	2.514 \pm 1.369	0.430 ^a	0.171
Nanning	22.82°N, 108.35°E	2017	2.541 \pm 1.376	2.000 ^a	0.787
Tazhong	39.00°N, 83.67°E	2017	0.047 \pm 0.028	0.700 ^a	14.903
Zhengzhou	34.78°N, 113.68°E	2017	7.017 \pm 3.765	4.880 ^a	0.695
Akdala	47.12°N, 87.97°E	2017	0.112 \pm 0.053	0.450 ^a	4.035
Urumqi	43.21°N, 87.12°E	Aug 2016–Jul 2017	0.191 \pm 0.113	0.520 ^b	2.720
Astore	35.21°N, 74.48°E	2016–2017	0.321 \pm 0.142	2.100 \pm 0.700 ^c	6.534
Sost	35.52°N, 74.25°E	2016–2017	0.190 \pm 0.096	1.400 \pm 1.100 ^c	7.382
Gilgit	36.41°N, 74.49°E	2016–2017	0.308 \pm 0.127	2.400 \pm 0.600 ^c	7.801
QOMS	28.36°N, 86.95°E	May 2015–May 2017	0.441 \pm 0.237	0.299 \pm 0.341 ^d	0.677
Langtang	28.21°N, 85.61°E	Oct 2016–May 2017	0.799 \pm 0.337	0.482 \pm 0.273 ^e	0.602
New Delhi	28.58°N, 77.20°E	Jan, 2016–Dec 2018	11.488 \pm 5.788	13.575 \pm 8.401 ^f	1.182
Kolkata	22.65°N, 88.45°E	Jan 2016–Dec 2018	12.728 \pm 5.846	12.082 \pm 6.850 ^f	0.949
Bhuj	23.23°N, 69.66°E	Jan 2016–Dec 2018	0.582 \pm 0.294	2.021 \pm 1.471 ^f	3.471
Port Blair	11.66°N, 92.71°E	Jan 2016–Dec 2018	0.132 \pm 0.107	2.506 \pm 1.030 ^f	19.050
Pune	18.53°N, 73.85°E	Jan 2016–Dec 2018	4.162 \pm 2.053	6.955 \pm 6.436 ^f	1.671
Nagpur	21.10°N, 79.05°E	Jan 2016–Dec 2018	3.345 \pm 1.487	4.493 \pm 2.579 ^f	1.343
Ranchi	23.31°N, 85.31°E	Jan 2016–Dec 2018	5.518 \pm 2.328	4.416 \pm 2.202 ^f	0.800

^aGuo et al., 2020. ^bZhang, Zhao, et al., 2020. ^cZeb et al., 2020. ^dChen et al., 2018. ^eRai et al., 2019. ^fKumar et al., 2020.

the domain shows distinct seasonality with minimum and maximum during summer and winter seasons respectively, which is similar to previous studies (Adhikary et al., 2007; Kumar et al., 2012; Yang et al., 2018).

During winter, pronounced BC concentrations (reaching as high as $8 \mu\text{g m}^{-3}$) spotted along the IGP region extending from Lahore, Delhi, Kanpur, and Varanasi to the Kolkata region are likely due to intense biomass burning (Figure S2 in Supporting Information S1). Additionally, shallow wintertime PBLH suppressed the vertical diffusion thereby trapping BC near the surface (Pan et al., 2015). Whereas, in China, higher demand for residential heating and carryover effect of industrial production at the end of the year leads to higher BC emissions during winter (Lu et al., 2011). Distinctive westerly winds at 500 hPa prevailed in the 20°–40°N latitudinal section in winter, where the highest BC mass concentrations were also observed which is probably due to low wind speeds and dynamic circulation patterns. During spring and summer, the higher concentrations over IGP are marked in two identical locations namely Kolkata and Lahore. Compared with other seasons, summer has low BC concentration throughout the entire domain as the onset of monsoon facilitates the wet removal process. According to Bates et al. (2006), the aerosol removal process plays an important role in the seasonal distribution and is a significant cause of uncertainty in model predictions. In Figure 4, high precipitation over SA and East Asia (EA) during monsoon season results in less BC concentration due to wet scavenging by precipitation. In autumn, a post-monsoonal transition period, during which monsoon retreats and wind direction shifts, both favors an increase in BC concentration.

For comparison, the mean and standard deviation of measured and model BC concentration from 23 sites are provided in Table 5, showing higher BC concentrations in urban than background sites. The simulated BC

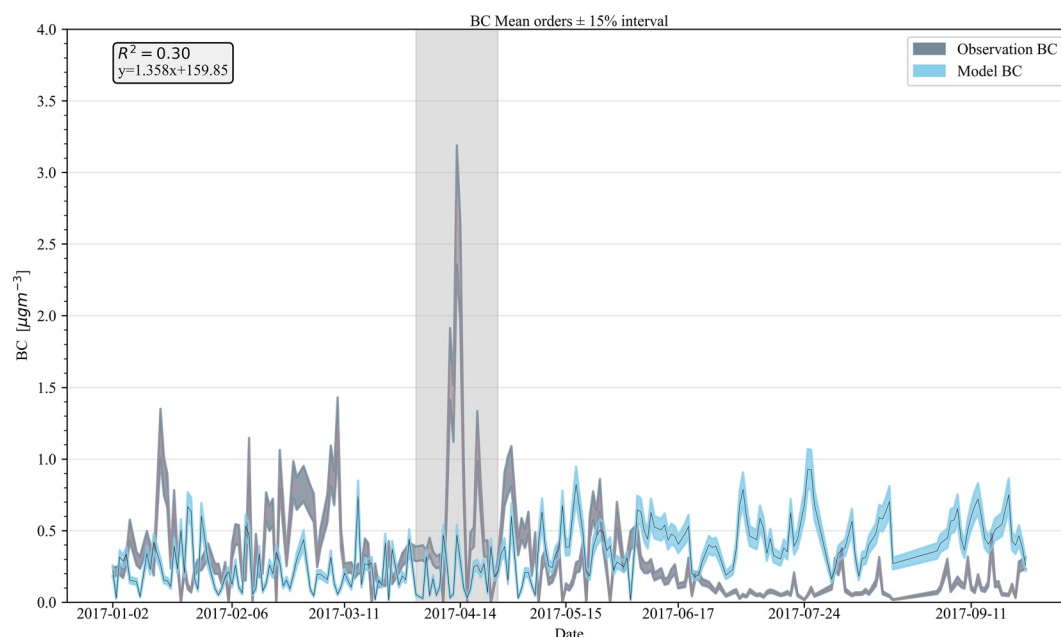


Figure 7. Time series of simulated (black) and observed (orange) black carbon (BC) at the Qomolangma Station (QOMS) for the period of January–September 2017. Gray and blue colors show BC mean values orders in ($\pm 15\%$) intervals. Vertical shaded gray color indicates an episodic event observed during the spring season.

concentrations exhibit high value in Kolkata ($12.728 \pm 5.846 \mu\text{g m}^{-3}$) and New Delhi ($11.488 \pm 5.788 \mu\text{g m}^{-3}$) followed by Chengdu ($7.375 \pm 4.098 \mu\text{g m}^{-3}$) and Beijing ($5.866 \pm 4.059 \mu\text{g m}^{-3}$). In contrast, relatively low surface BC concentration was found in the remote sites, such as Tazhong ($0.047 \pm 0.028 \mu\text{g m}^{-3}$), Port Blair ($0.132 \pm 0.107 \mu\text{g m}^{-3}$), Lhasa ($0.206 \pm 0.117 \mu\text{g m}^{-3}$), Gilgit ($0.308 \pm 0.127 \mu\text{g m}^{-3}$), QOMS ($0.441 \pm 0.237 \mu\text{g m}^{-3}$), and Langtang ($0.799 \pm 0.337 \mu\text{g m}^{-3}$). Figure 7 shows the simulated and observed daily mean BC concentrations at the QOMS site. During the simulated period, the observed and simulated daily mean data at the QOMS site were $0.307 \pm 0.257 \mu\text{g m}^{-3}$ and $0.286 \pm 0.179 \mu\text{g m}^{-3}$, respectively. These values are close to earlier findings of $0.250 \pm 0.220 \mu\text{g m}^{-3}$ (Cong et al., 2015) and $0.299 \pm 0.341 \mu\text{g m}^{-3}$ (Chen et al., 2018). At the QOMS site, BC seasonality was evident with the lowest and highest concentration during monsoon ($0.128 \pm 0.101 \mu\text{g m}^{-3}$) and spring ($0.431 \pm 0.385 \mu\text{g m}^{-3}$), respectively. However, the model was overestimated by the magnitude of 4 during the monsoon season. In contrast, during pollution events in spring, the modeled BC concentrations were underestimated by a factor of ~ 2 . The discrepancy found here could be caused by numerous factors such as emission inventories, topography, model resolution, and parameterizations schemes. The results from relatively coarser resolution could not adequately represent the special local events (biomass burning) and wet removal process that ultimately led to cause in model biases. In our study, the correlation coefficient between the model and observed BC at QOMS site was found to be 0.30, whereas Gul et al. (2021) study from Himalaya (Yala glacier; 4,900 m a.s.l) also found the correlation coefficient in a close similarity (0.32). As shown in Table 5, the model underestimated the BC concentration in most of the locations. The Port Blair, being far from the emission source, the high mean ratio value indicated the model underestimation and raised the concern on the model's ability to reproduce in the background region. Similarly, Pan et al. (2015) also found significant BC underestimation in Port Blair where the model captured only about 10%–38% of the observed values. Even with fine resolution, a study from Mues et al. (2018) shows strong underestimation by the model in Kathmandu, Nepal. It is noteworthy to mention that BC underestimation by chemical transport model has been a common problem in the IGP region (Joshi et al., 2016), EA (Gao et al., 2014), SA (Kumar et al., 2015; Nair et al., 2012), and TP (Ji, 2016). Such discrepancy in the model could originate from different uncertainties such as inadequate representations of emissions data, model resolution, representation of planetary boundary layer height, and general features of geography (Alvarado et al., 2018; Kumar et al., 2015; Pan et al., 2015). However, by comparing our results with the available observation data and the model simulation from previous studies, WRF-Chem can deliver with good agreement in reproducing seasonal, spatial variation, and magnitude in the surface BC concentration within the specified domain.

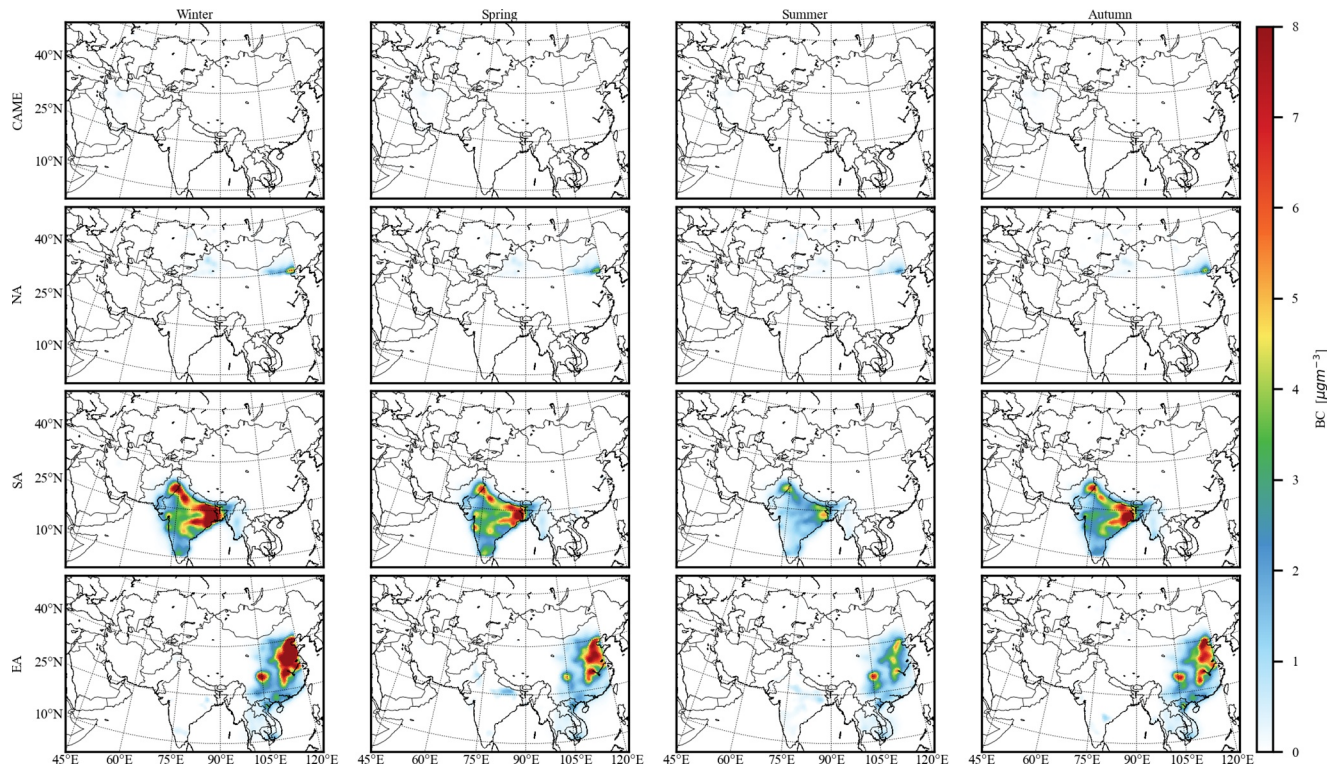


Figure 8. Spatial distribution of anthropogenic black carbon (BC) concentration ($\mu\text{g m}^{-3}$) emitted from East Asia (EA), South Asia (SA), North Asia (NA), and Central Asia and Middle East (CAME) on a seasonal basis.

3.3. BC Source Region and Transport Mechanism to the TP

3.3.1. Regional BC Contribution to TP

In this study, sensitivity analysis was carried out to quantify the contribution of anthropogenic BC to the TP from the surrounding subregion. For this, we analyzed the concentration and contribution of anthropogenic BC from different source regions of the domain as a part of the experimental design in Table 2. The results presented in Figure 8 are the product of the control minus sensitivity experiments, which clearly show a strong dependence of BC concentration with both seasonality and locality. The seasonal relative contribution from each neighboring region to the whole domain and toward TP is presented in Figure 9. During the simulation period, fractional BC

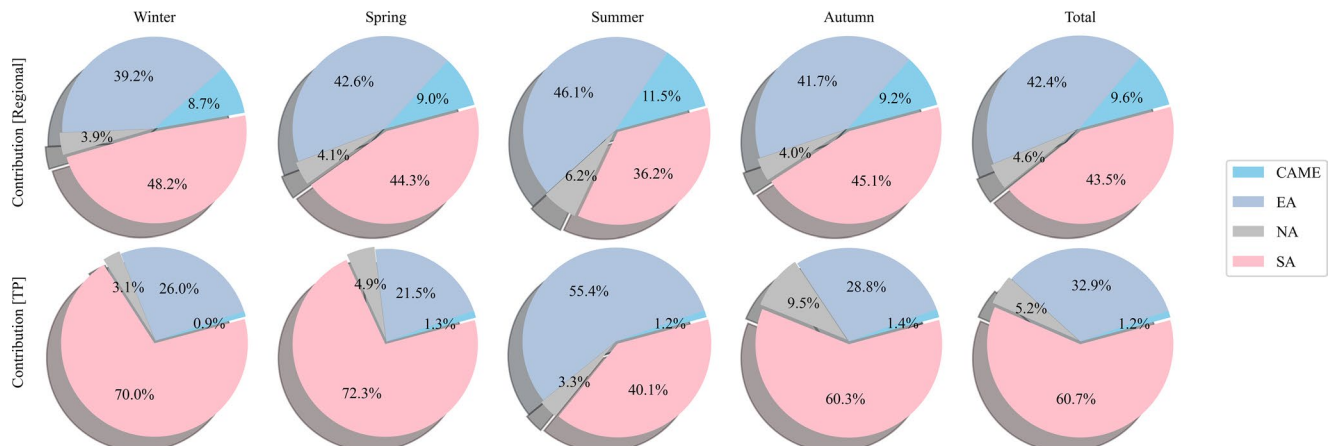


Figure 9. Relative seasonal and total black carbon contribution (%) to the whole domain from the surrounding subregion (First row) and toward Tibetan Plateau (TP) (second row). Different colors represent the different regions as given in the legend.

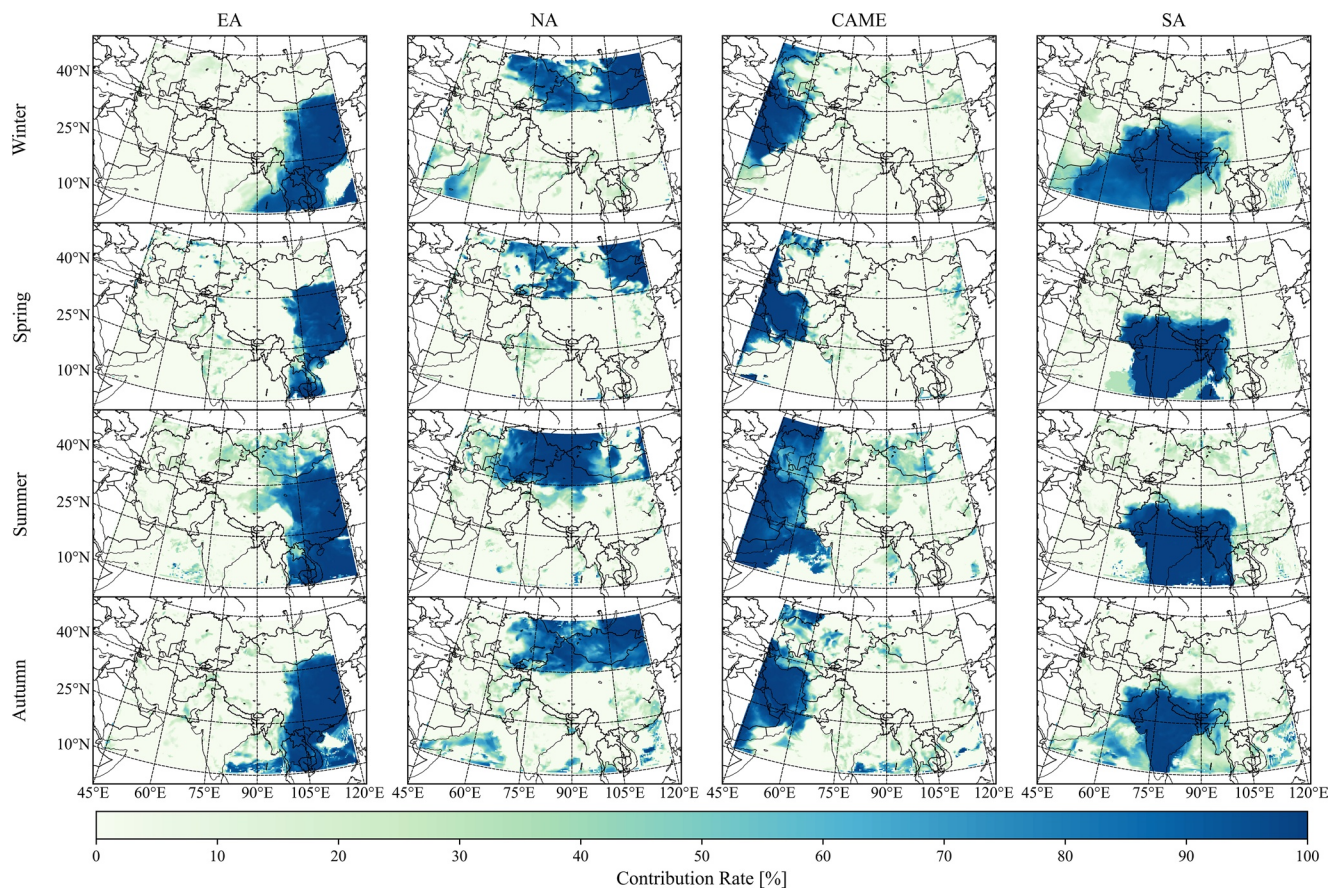


Figure 10. Spatial distribution of percentage contribution of anthropogenic BC from subregions. Row and column represent seasons and region respectively.

contributions concerning the whole domain from SA, EA, CAME, and NA are found to be 43.5%, 42.4%, 9.6%, and 4.6%, respectively. Of the total BC emissions, SA contributed higher than EA, however, in terms of BC contribution to TP, the contribution from SA (60.7%) is found to be twice that from EA (32.9%). As described in Lu et al. (2012), the smaller contribution from EA could be associated with the geography where high BC flux areas including eastern and central China are mostly downwind of the TP, and only the EA summer monsoon can effectively bring aerosol from EA to the TP. Especially, during the dry period, that is, winter (70.0%) and spring (72.3%) seasons, the stronger SA contribution to TP is evident. This may be modulated by the extensive biomass burning over the period in that region (Figure S2 in Supporting Information S1). During the summer monsoon, BC contribution from SA significantly dropped (almost by about 30%) partly due to efficient wet removal of BC by precipitation (Figure 4) and decreased forest fire events (Figure S2 in Supporting Information S1). Additionally, atmospheric circulation could have also played a vital role where the predominant south-westerly wind changes the direction as wind speed weakens (Figure 5) which ultimately inhibits the BC transport from SA. The contribution from EA peaks high (55.4%) during summer (EA contribution remains <30% in the rest of the seasons). Such seasonality in fractional contribution from SA to the TP is also stated by Zhang et al. (2015) and Han et al. (2020). In addition, Yang et al. (2018) also suggested the same, but it is worth mentioning here that this study included October–April and May–September as non-monsoon and monsoon seasons, respectively.

From a regional perspective, SA and EA observe high BC concentration (Figure 8) which propagated higher contribution from these regions (Figure 9). In terms of affected areas over TP, BC outbreak from SA influences largely than any other neighboring region (Figure 10). This could be due to the proximity of geographic location and circulation patterns under prevailing south-westerlies conditions. Additionally, Han et al. (2020) found that the strong biomass burning in SA greatly enhanced surface BC concentrations in the TP. Thus, it may be associated with the biomass burning activities over the SA region that could affect to a larger extent.

The TP region remains relatively clean throughout the year, with only 10% (Zhang et al., 2015) and 13.5% (Zhao et al., 2021) of BC being contributed from local emissions over the HTP. Inferring to this, a large portion of BC invades into TP from distance sources that need to be accounted for. Present study findings suggest that surface BC in the TP is mainly originated from SA and EA. Kumar et al. (2012) study showed that anthropogenic emissions substantially influence (up to 60%–96%) of the total BC loading over SA that was further proven by an evidence-based previous study based on the Aerosol Robotic Network (AERONET) and the Moderate Resolution Imaging Spectroradiometer (MODIS) fire count data (Ramachandran et al., 2020; Xu et al., 2018). A large portion of anthropogenic BC comes from agricultural waste burning emissions over SA (Xu et al., 2018). Whereas, over the Himalayas, Li et al. (2016) found that 54% and 46% BC contributions were from biomass and fossil fuel combustion, respectively. Over CA, Kulkarni et al. (2015) revealed averaged BC concentration was about $0.1 \mu\text{g m}^{-3}$, with peak values ($\sim 1 \mu\text{g m}^{-3}$) in the winter. A study performed by Xu et al. (2018) shows the BC concentrations range from 0.1 to $5 \mu\text{g m}^{-3}$ along the foothills of the Himalayas. Comparatively, the BC contribution (from SA) to the TP is in general agreement with previous findings by Lu et al. (2012) (67%), Zhang et al. (2015) (50%), and Yang et al. (2018) (61.3%). Although EA contribution is comparable with Han et al. (2020) (35%), noticeable differences were found from other previous studies, by Lu et al. (2012) (17%), by Zhang et al. (2015) (19%), and by Yang et al. (2018) (<10%). Such discrepancies could be caused by the definition of geographic boundary to TP and subregion, circulation pattern, and the methods adopted to calculate relative contribution to TP from respective subregion.

3.3.2. Columnar BC, Transport Flux, and Mechanism

BC at atmospheric vertical regime allows us to better understand columnar BC mass concentration and transport mechanism involved within the atmospheric layer. To gain insight into the topographic effect on transport mechanism, we presented vertical BC distribution from sensitive analysis (Figure 11) along with terrain height. Considering the topographic effect on BC transport, we took transect in such a manner where the two most polluted IGP and EC regions fall in-between. In this study, columnar profile exhibits BC injected to the higher elevation where the presence of BC was found to be up to an elevation of about 6-km over SA and EA, which is similar to previous finding (Yuan, Wan, et al., 2020; Zhang et al., 2015, 2017; Zhang, Zhao, et al., 2020; Zhao et al., 2017). However, the overall picture illustrated in Figure 11 confirms the topographic barrier effect on BC distribution where the higher BC concentration ($1.4\text{--}2 \mu\text{g m}^{-3}$) is confined in the valley-type topography within a 2-km altitudinal distance from the surface. The previous studies on the natural barrier effect by towering the Himalayas from the southern flank of TP and EC are understandable. Zhao et al. (2017) found that the significant enhancement of BC transport with the reduction of the Himalayas altitude under the influence of the convergent airflows condition significantly increased BC over southeastern TP. Whereas, Zhang et al. (2017) suggested that due to the presence of high altitude cut-off low system, pollutant enhanced to TP by a factor of 6. Similarly, Gong et al. (2019) and Zhang, Zhao, et al. (2020) found that the mountain valley system increased the transport flux by three times and 50%, respectively. Our study shows the higher BC contribution to TP (Figure 9) and larger affected area (Figure 10) from SA and EA regions. Despite the fact of the wet removal process, BC was found to be uplifted in the higher atmospheric column that could be modulated by the deep convection process when hit by the summer monsoon over the SA (Figure 11, summer). The high BC distribution was experienced in the latitudinal cross section of $20^{\circ}\text{--}27^{\circ}\text{E}$ and $31^{\circ}\text{--}112^{\circ}\text{E}$ in the southern and eastern slope of TP. During summer, a distinct feature of vertical dispersion occurred over SA and EC that could be governed by a monsoonal activity and deep convection process, which could form a critical pathway to TP that permits BC to enter from the surface to the upper layers. Thus, it can be inferred that the role of monsoonal activity is not only limited to the wet removal process but also plays a vital role in opening the window for the vertical dispersion of pollutant. Singh et al. (2020) study on dynamical forcing in vertical BC transportation also showed that the persistent BC layer observed at the free troposphere layer resulted from uplifted BC during the convective period from SA. As explained by Yuan, Chen, et al. (2020), high BC over the east slope of TP resulted from the weakness of westerly winds over the northern TP, eastward movement of EA major trough, and dominant westerly wind over southern TP. Such a circulation pattern along with trans-Himalaya transport through mountain-valley conduits systems (Khumbu valley, Dudh Koshi basin, Kali Gandaki, Langtang valley, Chumbi valley, and Yarlung Tsangpo Grand Canyon), through which BC could have made way up to the TP (Dhungel et al., 2018; Yuan, Wan, et al., 2020; Zhang, Zhao, et al., 2020).

Further, we have quantified the BC transport flux along height-cross section. We have investigated on the BC flux distribution under different wind regimes, and calculated BC flux taking into consideration of different

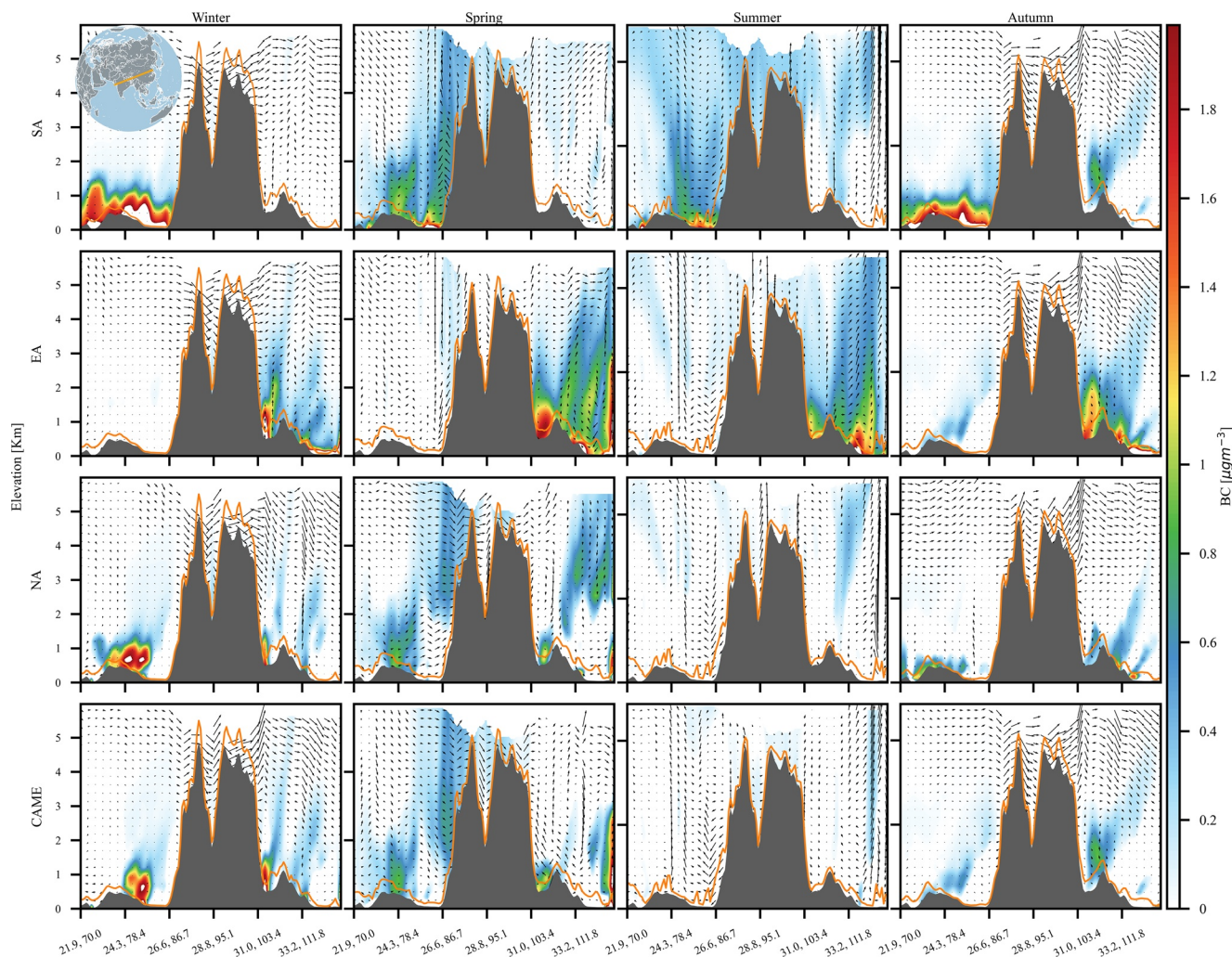


Figure 11. Cross-section of regional columnar black carbon mass concentration. The filled gray color indicates terrain height (topography) and the yellow line denotes seasonal planetary boundary layer height. In the left upper corner, a straight yellow line shows the starting and ends of a cross section.

wind fields in Figure 12 (a-meridional, b-vertical, and c-wind speed). The predominant southwesterly meridional wind system favor BC aloft at a significant rate ($2\text{--}3 \mu\text{g m}^{-2} \text{s}^{-1}$) over SA due to high meridional wind (6 m s^{-1} ; Figure 12a). In Figure 12b, we found the vertical wind played an important role on BC transport to the TP. It shows that the deep convection transport is influenced by vertical wind where elevated transport flux is dominant over SA and EA regions. Moreover, BC flux can be seen over the HTP region in the range from 0.015 to $0.025 \mu\text{g m}^{-2} \text{s}^{-1}$. Similarly, Figure 12c exhibits wind speed-induced BC flux. Despite high BC flux located over SA and EA, a significant BC flux over HTP and beyond might have due to the fact of updraft effect. Figures 12a–12c shows BC transported to the upper troposphere and lower stratosphere (UTLS) that could potentially be driven by deep stratospheric intrusion under the strong wind speed. Thus, we suggested that the different wind regime has an essential impact on the horizontal and vertical transport of pollutants as the fate of short-lived pollutants like BC accumulation and dispersion. Here, different BC flux rates resulted vary with each wind component thus, it calls for the consideration of these wind fields while evaluating aerosol transport and calculation of transport flux.

As the columnar distribution of BC also depends on the variation of the PBLH profile. Hence, here we provide a dynamic evolution of the cross-sectional PBLH profile that shows a clear seasonal variation (Figure 11 yellow line). In winter and autumn, shallow PBLH over SA and part of the IGP region ($20^{\circ}\text{--}27^{\circ}\text{E}$) suppresses ventilation thereby trapping the lower atmospheric BC within $\sim 1\text{-km}$. On contrary, during spring and summer, PBLH was found to expand, which is likely due to the underlying surface warming process thereafter initiating thermal

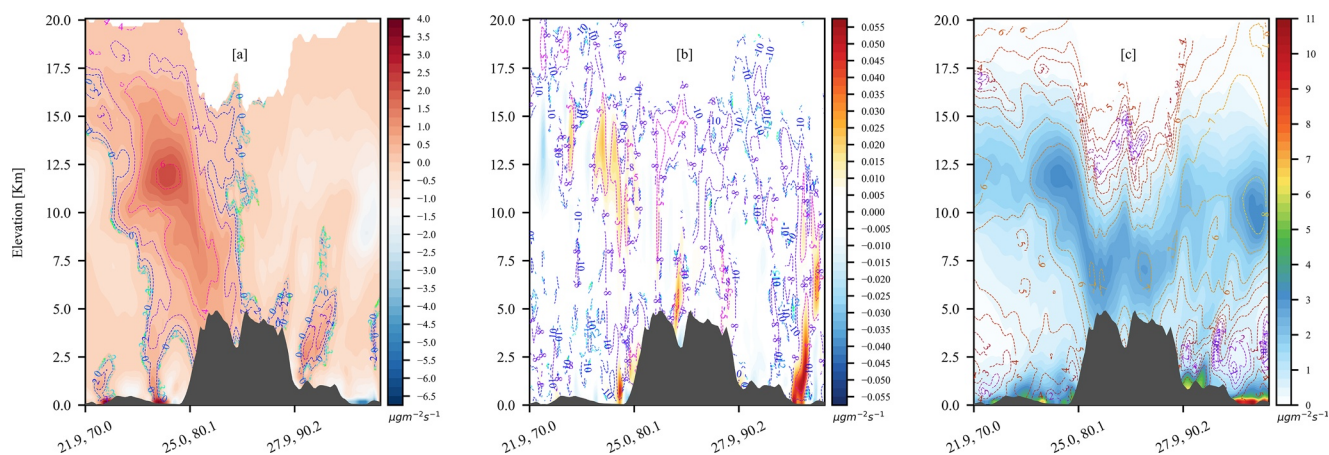


Figure 12. Height-Cross-sectional black carbon transport flux calculated along the line (as shown in yellow solid line in Figure 12) with meridional (a), vertical (b) wind component, and wind speed (c).

instability that later strengthens PBLH and facilitates vertical diffusion. To provide additional evidence on a complex interplay of aerosol-boundary layer interaction, we have analyzed the zonal mean PBLH change caused by aerosol change by compared with the control and sensitivity experiments (Figure 13). In particular, we showcase the synergy between BC and associated mechanisms in modifying PBLH. Figure 13 illustrates that the higher PBLH in control than sensitivity experiments implying to this BC further enhance in PBLH development. Our finding showed that BC expand PBLH by 5.0% and 4.8% over SA and EA regions, respectively. Such PBLH increment is comparable with Wang et al. (2018) (4%–6%), however, higher than Slater et al. (2021) (0.26%). On contrary to these findings, Ding et al. (2016) suggested BC could decrease the PBLH, though this study only shows the effect of BC at and above PBLH top. Supporting this, Slater et al. (2021) stated that BC high above the PBLH has little impact on PBLH development. Whereas, Wang et al. (2018) stated that near surface BC tends to promote the PBLH development thus in our case as well maximum BC concentrations limited within near surface (<1 km) that could potentially facilitated growth of PBLH. Unlike other aerosols species, BC at surface absorbs the downwelling radiations, which increase turbulent kinetic energy that led to PBLH expansion thereby facilitates BC dissipation through promoting atmospheric buoyant turbulence. However, it is noteworthy to mention that BC concentrations, vertical profile of BC, mixing state, and underlying land surface play a crucial role on PBLH change in association of aerosol-boundary layer interaction (Slater et al., 2021).

As stated by Huang et al. (2020), BC could play an important role in aerosol-boundary layer interaction which consequently intensifies lower atmospheric pollution. The effect of BC on the PBLH is very sensitive (Ding et al., 2016), thus we have explicitly elucidated the complex interplay of aerosol-boundary layer interaction that is inherently connected to air pollution by modulating through accumulation, dispersion, turbulent mixing, efficient dilution, as well as transportation process (Wang et al., 2018; Zhao et al., 2020). Thus, under the given circumstances, we speculate that, apart from elevation-dependent and mountain valleys transport, the presence of BC at the vertical regime and transport toward the TP may also depend on convective transport mechanism (Bian et al., 2020), circulation mode (Yuan, Chen, et al., 2020), and meridional flow (Xu et al., 2014). In addition to this, we emphasize taking into consideration of aerosol-boundary layer interaction while analyzing the above-mentioned process. The driving force for BC transport from the neighboring region to TP is discussed in detail in the following section.

3.3.3. Footprint Analysis: A Source-Receptor Examination at QOMS Site

Tracing potential sources of air parcels further aid in identifying the source of BC. In doing so, here we present a case study on footprint analysis at the QOMS site (Figure 14 and Figure 15). The pollutant enrichment at the background site like the HTP is linked with the long-range transport (Gabielli et al., 2020; Han et al., 2020; Kopacz et al., 2011), thus here we further provide evidence on potential sources and long-range transport mechanism at QOMS site. In Figure 14, the majority of air masses arriving at the QOMS site are from a long-range and higher elevation, suggesting prevailing westerlies throughout all seasons except monsoon which is also supported by

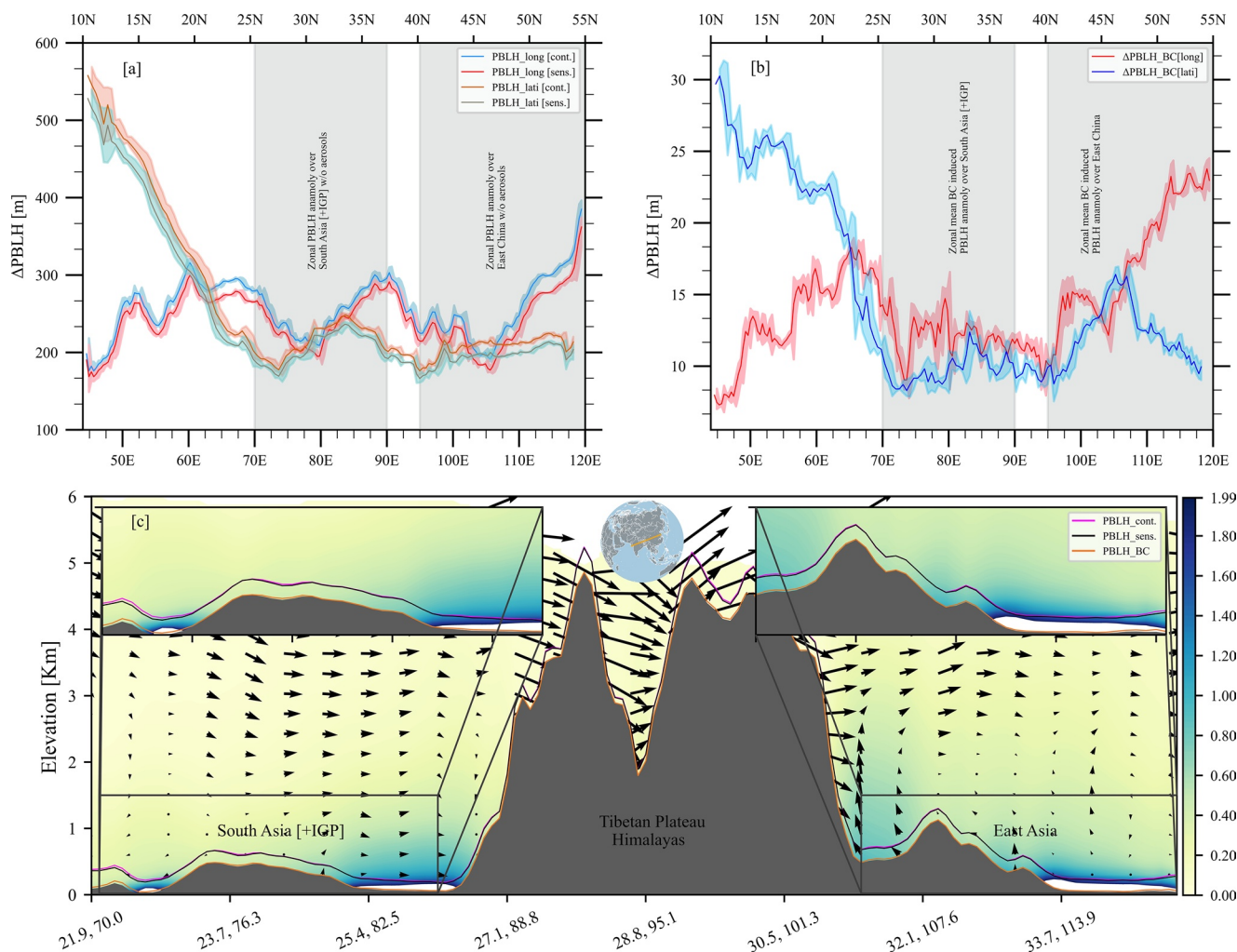


Figure 13. Zonal mean aerosol induced planetary boundary layer height (PBLH) changed for control and sensitivity experiment (a), latitudinal (blue line) and longitudinal (red line) BC-induced PBLH change (b), same as Figure 11 but with annual mean BC concentrations where purple, black, and orange line indicates PBLH for control, sensitivity, and due to BC. In upper panel (a) and (b), the solid line shows change in zonal mean (Δ PBLH) whereas identical shadowed part indicated $\pm 1\sigma$. The shaded gray color indicates the PBLH anomaly from control and sensitivity experiment (a), due to BC over South Asia (SA) and East Asia (EA) (b), and terrain height (c). The inset area in left and right represents the SA and EA regions.

Figure 5. From cluster analysis, it can be seen that a large portion of air masses received from the CAME region during winter and spring. However, during monsoon and autumn, the strong SA monsoon and the post-monsoon effect are vivid as the higher density air masses arriving at QOMS are from a relatively lower elevation that mainly originated from the BOB as each of the seasons accounts for about 90% and 80% of air masses. Especially during monsoon, such bulk number of air masses could aloft BC from lower to higher elevations through convection process and mountain-valley ventilation channel and further transport horizontally to TP.

The QOMS site is known to have been influenced by a significant contribution from long-range transport (Chen et al., 2018; Pokharel et al., 2019). To explore the connection between an episodic event (Figure 7) and the potential source of BC transport pathways, here we quantified the contribution fraction and frequency of occurrence through PSCF analysis. From Figure 15, our results suggested that the high fraction of BC contributed from CAME and SA region. The footprint of strong long-range transport can be seen during winter and spring, which traced back to the Middle East, Central Asia, Afghanistan, Pakistan, Nepal, and IGP region. Interestingly, it was found that the fractional contribution of BC at the QOMS site is reduced by half during monsoon and autumn than in the winter and spring seasons. This could be possibly linked with the wet removal process, this phenomenon further was proved by Figure 4, where higher precipitation was seen during monsoon than that during the

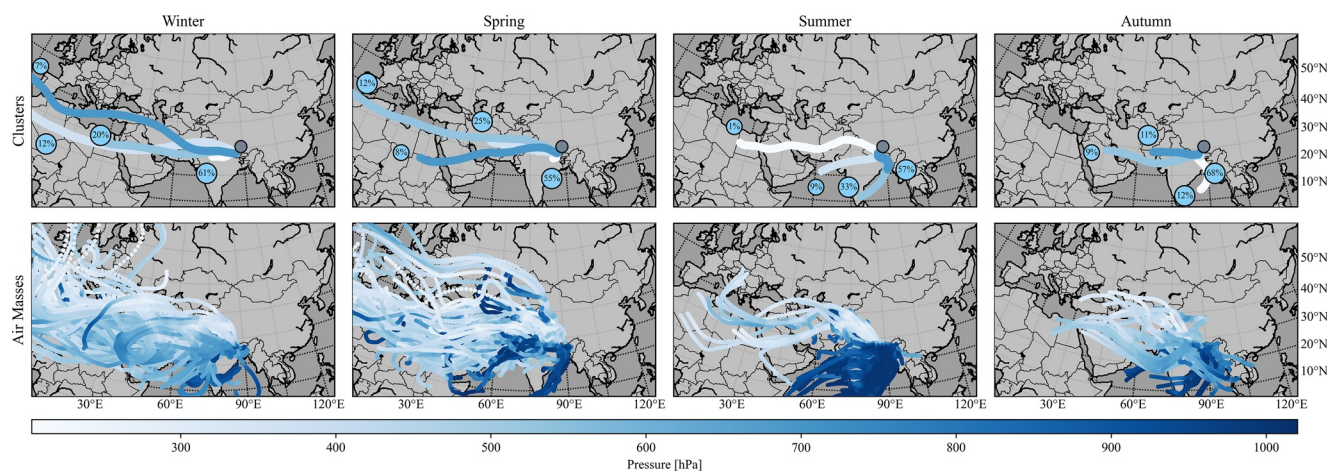


Figure 14. Seven days backward trajectories of air masses (upper panel) and clusters (lower panel) generated by the HYSPLIT model at the QOMS site during the simulation period. Dark circular gray color indicates receiving (QOMS) site. The pressure height (hPa) is shown by color-coding.

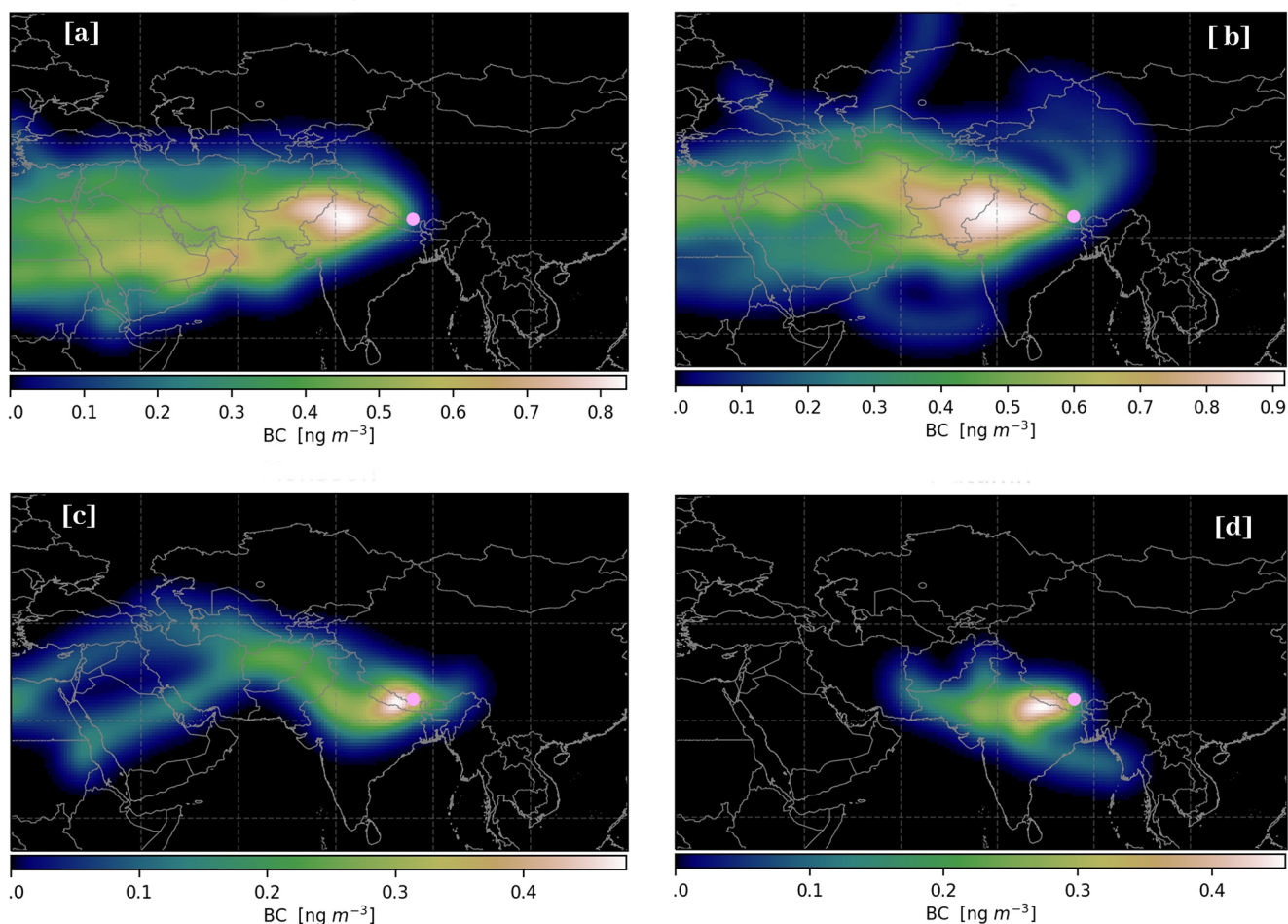


Figure 15. Seasonal (a-winter, b-spring, c-summer, and d-autumn) potential source contribution function (PSCF) at QOMS site. Gray circle showing the measurement site.

non-monsoon season. The BC concentration during an episodic event is maximum than the average background concentration, reflecting the possibilities of import from a distance source.

As shown in Figure 15 (spring), this pollution event might have occurred due to the long-range transport. The polar plot (Figure S3 in Supporting Information S1) shows that up to 40% of BC received at the QOMS site comes from the west and southwest during winter and spring, while during monsoon and autumn season, the contribution from the west comes down to 20%–30%. Apparently, during the monsoon, a small contribution from east and southeast was also observed at the QOMS site, this could have brought by the Southeast Asian circulation pattern (Figure 5). This finding is in agreement with the previous studies (Bianchi et al., 2021; Lüthi et al., 2015), thus, we conclude that the significant BC contribution to TP (at the QOMS) site is driven by long-range transport mechanism making way along cross-mountain pathways through mountain-valley channel system.

3.4. BC Radiative Forcing and Response in Temperature

Depending upon the place and process, BC concentration may vary, thereby causing radiative perturbation. We calculated Radiative Forcing (RF) and temperature change from BC's direct effect. Figure 16 illustrates the direct RF pattern, showing more negative surface RF (up to -8 W m^{-2}) over EA. Of which, the strongest negative RF occurred over the high BC loading region like Northeast China and Chengdu, implying BC cooling effect at the surface. Over this region, RF distribution is in line with the previous studies (Gao et al., 2014; Yang et al., 2018; Zhao et al., 2014). Whereas, over TP and Himalayas, BC-induced forcing is in the range of -1 to 2 W m^{-2} , which is consistent with previous studies (Ji, 2016; Yang et al., 2018). The positive value of the radiative effect signifies warming due to BC. In addition, He et al. (2014) found the surface dimming effect due to BC (-4.7 W m^{-2}) over TP. Similarly, the Himalayas as background condition, Marcq et al. (2010) found surface RF of about -1.5 W m^{-2} , but the notable difference also observed based on the season and underlying surface. In contrast, despite high BC over SA, less negative surface RF might be due to several factors like the underlying surface regime, cloud adjustment effect, sensible heat (SH), and latent heat (LH). Zhang, Chen, et al. (2020) explicitly stated that BC-induced direct RF varies under the meteorological influence and different climate regions.

As argued by Song et al. (2019), a decrease in LH and SH fluxes compensates for surface radiative cooling, leading to a drop in surface temperature. Both the LH and SH (Figure S4 in Supporting Information S1) are more negative over EA than SA, thus it can be inferred that the effect of LH and SH will, in turn, reflect upon different surface RF over SA and EA. Ghosh et al. (2020) stated that BC-induced radiative perturbation is only responsible for 10%–20% of surface cooling over the IGP region. Our model simulation result shows more negative BC-induced temperature change is concentrated over EA, coincident with maximum negative surface RF. Similarly, over SA, the temperature change is positive, indicating a warming effect due to high BC concentration, LH, and SH. Over SA, high and low BC-induced temperature change occurred during winter and monsoon, as this monsoon sees maximum and minimum BC concentration, respectively. The previous studies by Ji (2016) (0.1 – 1.5°C), Yang et al. (2018) (0.08°C), and Xu et al. (2016) (1.3°C) found significant BC-induced warming effects over the TP region. Similarly, over the Himalayan range, Ménégoz et al. (2014) found BC-induced localized warming between 0.05 and 0.3°C . Compared with these studies, our finding also shows a similar pattern with the highest BC-induced temperature change during spring (0.15°C). However, the maximum annual mean temperature change goes up to 0.06°C (Figure S4 in Supporting Information S1). In addition to this, BC-induced temperature change profile (Figure 16, third column) shows seasonal latitudinal and longitudinal mean temperature change ranges from -0.1 to 0.1°C . Both latitudinal and longitudinal means shows more warming trend over the TP region especially during winter, spring, and autumn. The significant BC-induced warming over the TP is a matter of high interest. The notable warming feature of BC response particularly over the TP and Himalayas cannot be neglected as these regions provide tangible cryospheric services, and play an important role in driving hydrological and atmospheric cycle, and environmental processes.

4. Conclusions

In this study, we employed the WRF-Chem model for the quantitative assessment of atmospheric BC concentration, contribution, aerosol-boundary layer interaction, BC transport flux, and transportation over PTP. Taking advantage of available reanalysis products and observation data, first we validated the model performance, then investigated spatiotemporal/columnar distribution and transportation of BC, examined synergy between

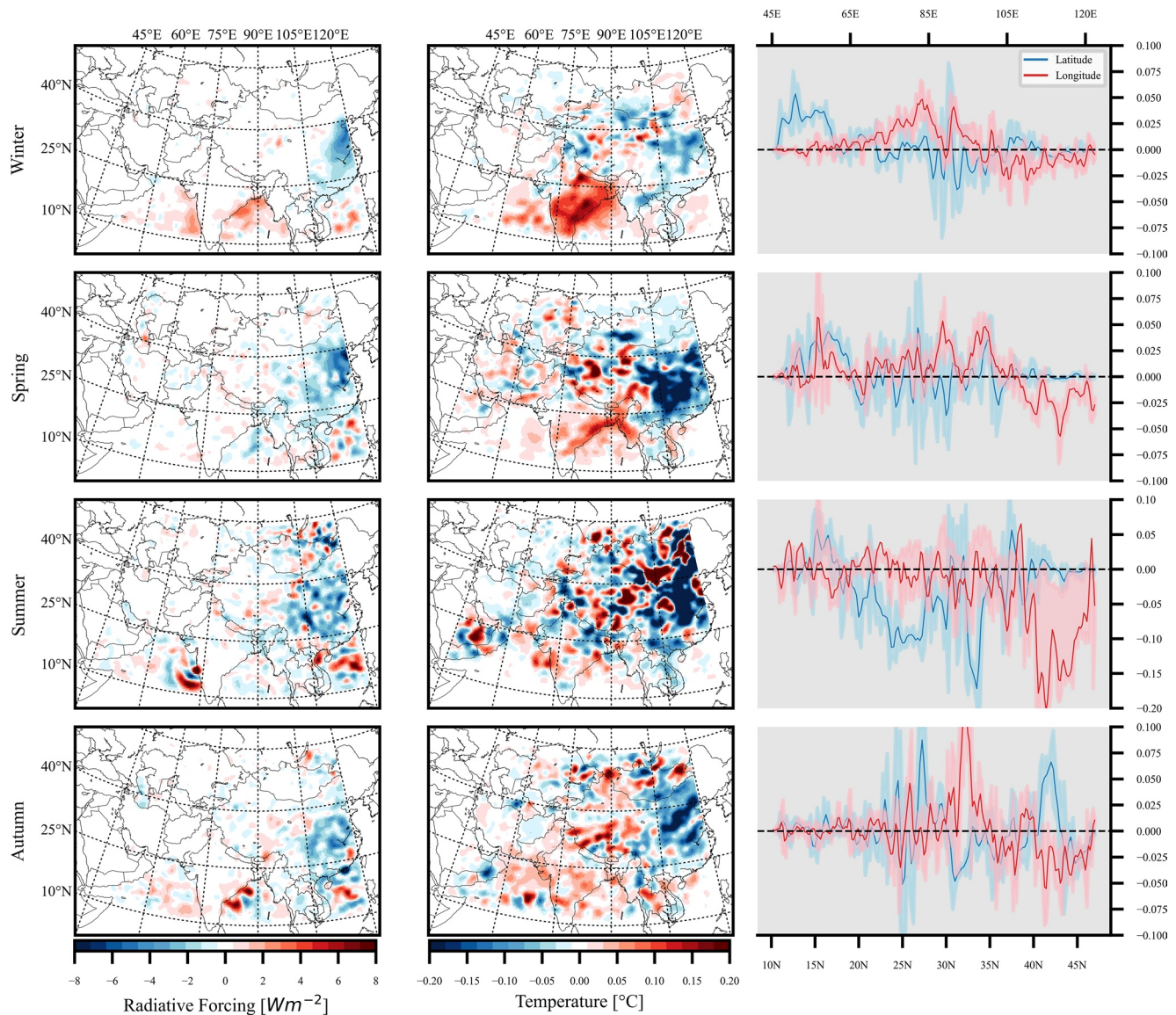


Figure 16. Seasonal-spatial distribution of surface radiative forcing (left column) and corresponding seasonal surface temperature change (middle column), and cross-sectional change in mean temperature (third column). In the third column, solid gray and blue line indicates the zonal mean (control-sensitivity) temperature change throughout longitude and latitude cross section, respectively. Similarly, shaded identical light pink, and light blue colors show $\pm 1\sigma$ denoted by shaded area.

aerosol-boundary layer feedback, calculated BC transport flux, analyzed source-receptor analysis, and assessed BC-induced direct RF and temperature change. We found a distinctive seasonal BC pattern with winter and spring high, and monsoon and autumn low. The BC concentration appears to be closely related to the strength of the emission source with higher values reaching up to $8 \mu g m^{-3}$ in identical hotspot regions (i.e., IGP, Chengdu, and EC). An efficient vertical transport up to 6-km was observed, which was more noticeable during the summer monsoon season over SA. However, the higher density of columnar BC was limited to 2-km in winter. Investigation on BC transport flux results showed that the significant BC flux enters into the upper troposphere and lower stratosphere (UTLS), which is mainly driven by the deep stratospheric intrusion process under the influence of strong wind speed that is dominant over SA and EA. BC transport flux over the TP was estimated in the range of $0.5\text{--}1.5 \mu g m^{-2}s^{-1}$, $0.01\text{--}0.025 \mu g m^{-2}s^{-1}$, and $1\text{--}3 \mu g m^{-2}s^{-1}$, respectively, driven by meridional, vertical wind field, and wind speed. Interestingly, our results on aerosol-boundary feedback interaction showed that BC expanded PBLH by 5.0% and 4.8% over SA and EA, respectively, which could eventually facilitates BC dispersion and transportation.

We also quantified the BC contribution from subregion to TP by conducting sensitivity analysis. Dominant BC to TP mainly originated from SA (60.7%), about twice EA (32.9%). Despite high BC over EA, the influence of BC on TP is subdued by circulation pattern, as TP is located in the upwind of EA. Seasonally, except for the summer monsoon, the contribution from SA sees high attribution in the range of 40.1%–72.3%, followed by EA, ranging from 21.5% to 55.4%. In contrast, only a small portion (<10%) of BC was contributed from NA and CAME regions. This could be due to geographic location, meteorological influence, and BC emission itself.

The results from footprint analysis at a typical TP site proved the long-range transport from the west and southwest source regions. Interestingly, the fractional contribution of BC at the QOMS site is reduced by half during wet seasons in comparison to dry seasons. Depending on the subregion underlying surface, BC-induced radiative perturbation shows a strong dimming effect over EA (-8 Wm^{-2}), which further corroborates with temperature change. Over TP, BC-induced warming was found to be maximum during high BC loading seasons, reaching high during spring (0.15°C). However, the annual mean BC-induced temperature change goes up to 0.06°C . Such temperature change is a matter of concern from the atmosphere-cryosphere point of view that needs to take into consideration in future perspectives. Thus, we conclude by noting that the trained model delivers satisfactory results in the regional context. However, we acknowledge the potential reasons for the bias issued in our study. It includes resolution of the model and meteorological forcing, parametrization scheme (PBL and land surface), detail feedback mechanism, and emission data. Given this, our study warrants further investigation.

Data Availability Statement

Meteorological observation data are available at (<https://www.wunderground.com/>), ERA-5 reanalysis data are available at (<https://cds.climate.copernicus.eu/>), temperature data can be accessed from (<http://www.cru.uea.ac.uk/data>), TRMM (3B42) precipitation data can be accessed from (<https://disc.gsfc.nasa.gov/>). NCEP data obtained from (<https://psl.noaa.gov/data/>). The WRF-Chem model used in this study can be accessed from (<https://ruc.noaa.gov/wrf/wrf-chem/>). The data and codes used in this paper can be accessed at <https://doi.org/10.5281/zenodo.6007286>.

References

- Adhikary, B., Carmichael, G. R., Tang, Y., Leung, L. R., Qian, Y., Schauer, J. J., et al. (2007). Characterization of the seasonal cycle of south Asian aerosols: A regional-scale modeling analysis. *Journal of Geophysical Research: Atmospheres*, *112*(D22).
- Alvarado, M. J., Winijkul, E., Adams-Selin, R., Hunt, E., Brodowski, C., Lonsdale, C. R., et al. (2018). Sources of black carbon deposition to the Himalayan glaciers in current and future climates. *Journal of Geophysical Research: Atmospheres*, *123*(14), 7482–7505.
- Bates, T., Anderson, T., Baynard, T., Bond, T., Boucher, O., Carmichael, G., et al. (2006). *Aerosol direct radiative effects over the northwest Atlantic, northwest Pacific, and North Indian Oceans: Estimates based on in-situ chemical and optical measurements and chemical transport modeling*.
- Bian, J., Li, D., Bai, Z., Li, Q., Lyu, D., & Zhou, X. (2020). Transport of Asian surface pollutants to the global stratosphere from the Tibetan Plateau region during the Asian summer monsoon. *National Science Review*, *7*(3), 516–533. <https://doi.org/10.1093/nsr/nwaa005>
- Bianchi, F., Junninen, H., Bigi, A., Sinclair, V., Dada, L., Hoyle, C., et al. (2021). Biogenic particles formed in the Himalaya as an important source of free tropospheric aerosols. *Nature Geoscience*, *14*(1), 4–9.
- Bolch, T., Kulkarni, A., Kääh, A., Huggel, C., Paul, F., Cogley, J. G., et al. (2012). The state and fate of Himalayan glaciers. *Science*, *336*(6079), 310–314.
- Bonasoni, P., Laj, P., Marinoni, A., Sprenger, M., Angelini, F., Arduini, J., et al. (2010). *Atmospheric Brown Clouds in the Himalayas: First two years of continuous observations at the Nepal Climate observatory-Pyramid* (5079 m).
- Bond, T. C., Doherty, S. J., Fahey, D. W., Forster, P. M., Berntsen, T., DeAngelo, B. J., et al. (2013). Bounding the role of black carbon in the climate system: A scientific assessment. *Journal of Geophysical Research: Atmospheres*, *118*(11), 5380–5552.
- Chen, F., & Dudhia, J. (2001). Coupling an advanced land surface–hydrology model with the Penn State–NCAR MM5 modeling system. Part I: Model implementation and sensitivity. *Monthly Weather Review*, *129*(4), 5692–6585. [https://doi.org/10.1175/1520-0493\(2001\)129<0569:CAALSH>2.0.CO;2](https://doi.org/10.1175/1520-0493(2001)129<0569:CAALSH>2.0.CO;2)
- Chen, H., Zhu, Q., Peng, C., Wu, N., Wang, Y., Fang, X., et al. (2013). The impacts of climate change and human activities on biogeochemical cycles on the Qinghai-Tibetan Plateau. *Global Change Biology*, *19*(10), 2940–2955.
- Chen, X., Kang, S., Cong, Z., Yang, J., & Ma, Y. (2018). Concentration, temporal variation, and sources of black carbon in the Mt. Everest region retrieved by real-time observation and simulation. *Atmospheric Chemistry and Physics*, *18*(17).
- Cong, Z., Kang, S., Kawamura, K., Liu, B., Wan, X., Wang, Z., et al. (2015). Carbonaceous aerosols on the south edge of the Tibetan Plateau: Concentrations, seasonality and sources. *Atmospheric Chemistry and Physics*, *15*(3), 1573–1584.
- Cross, M. (2015). *PySPLIT: A package for the generation, analysis, and visualizations of hysplit air parcel trajectories, paper presented at Proceedings of 14th Annual Scientific Computing with Python Conference (SciPy 15)*.
- Cucchi, M., Weedon, G. P., Amici, A., Bellouin, N., Lange, S., Schmied, H. M., et al. (2020). WFDE5: Bias adjusted ERA5 reanalysis data for impact studies. *Earth System Science Data Discussions*, 1–32.
- Davidson, C. I., Phalen, R. F., & Solomon, P. A. (2005). Airborne particulate matter and human health: A review. *Aerosol Science and Technology*, *39*(8), 737–749.

Acknowledgments

This study was supported by the Strategic Priority Research Program of the Chinese Academy of Sciences, Pan-Third Pole Environment Study for a Green Silk Road (Pan-TPE; XDA20040501), the National Natural Science Foundation of China (42071096), the State Key Laboratory of Cryospheric Science (SKLCS-ZZ-2021) and the Key Research Program of the Chinese Academy of Sciences (QYZDJ-SSW-DQC039). Mukesh Rai is supported by CAS-TWAS President's Fellowship for International Ph.D. students. We acknowledge matplotlib python package for making possible all the graphics used in our study (<https://matplotlib.org/>; Hunter, 2007). We are equally thankful to Cross (2015) for PySPLIT and Jean-Eudes Petit and Samuel Weber for pyPSCF modules.

- Derin, Y., & Yilmaz, K. K. (2014). Evaluation of multiple satellite-based precipitation products over complex topography. *Journal of Hydrometeorology*, *15*(4), 1498–1516.
- Dhungel, S., Kathayat, B., Mahata, K., & Panday, A. (2018). Transport of regional pollutants through a remote trans-Himalayan valley in Nepal. *Atmospheric Chemistry and Physics*, *18*(2), 1203–1216.
- Ding, A., Huang, X., Nie, W., Chi, X., Xu, Z., Zheng, L., et al. (2019). Significant reduction of PM 2.5 in eastern China due to regional-scale emission control: Evidence from SORPES in 2011–2018. *Atmospheric Chemistry and Physics*, *19*(18), 11791–11801.
- Ding, A., Huang, X., Nie, W., Sun, J., Kerminen, V. M., Petäjä, T., et al. (2016). Enhanced haze pollution by black carbon in megacities in China. *Geophysical Research Letters*, *43*(6), 2873–2879. <https://doi.org/10.1002/2016GL067745>
- Du, M., Liu, J., Li, Y., Zhang, F., Zhao, L., Niu, B., et al. (2019). Are high altitudinal regions warming faster than lower elevations on the Tibetan Plateau? *International Journal of Global Warming*, *18*(3–4), 363–384.
- Ek, M., Mitchell, K., Lin, Y., Rogers, E., Grunmann, P., Koren, V., et al. (2003). Implementation of Noah land surface model advances in the National Centers for Environmental Prediction operational mesoscale Eta model. *Journal of Geophysical Research: Atmospheres*, *108*(D22).
- Emery, C., Tai, E., & Yarwood, G. (2001). *Enhanced meteorological modeling and performance evaluation for two Texas ozone episodes*. Prepared for the Texas natural resource conservation commission. ENVIRON International Corporation.
- Emmons, L., Walters, S., Hess, P., Lamarque, J., Pfister, G., Fillmore, D., et al. (2010). Description and evaluation of the model for ozone and related chemical tracers, version 4 (MOZART-4). *Geoscientific Model Development*, *3*, 43–67. <https://doi.org/10.5194/gmd-3-43-2010>
- Fast, J. D., Gustafson, W. I., Jr, Easter, R. C., Zaveri, R. A., Barnard, J. C., Chapman, E. G., et al. (2006). Evolution of ozone, particulates, and aerosol direct radiative forcing in the vicinity of Houston using a fully coupled meteorology-chemistry-aerosol model. *Journal of Geophysical Research: Atmospheres*, *111*(D21).
- Feng, Y., Kotamarthi, V., Coulter, R., Zhao, C., & Cadet, M. (2016). Radiative and thermodynamic responses to aerosol extinction profiles during the pre-monsoon month over South Asia. *Atmospheric Chemistry and Physics*, *16*(1).
- Flanner, M. G., Zender, C. S., Hess, P. G., Mahowald, N. M., Painter, T. H., Ramanathan, V., & Rasch, P. (2009). Springtime warming and reduced snow cover from carbonaceous particles. *Atmospheric Chemistry and Physics*, *9*(7), 2481–2497.
- Frauenfeld, O. W., Zhang, T., & Serreze, M. C. (2005). Climate change and variability using European Centre for medium-range weather forecasts reanalysis (ERA-40) temperatures on the Tibetan Plateau. *Journal of Geophysical Research: Atmospheres*, *110*(D2).
- Gabrielli, P., Wegner, A., Sierra-Hernández, M. R., Beaudon, E., Davis, M., Barker, J. D., & Thompson, L. G. (2020). Early atmospheric contamination on the top of the Himalayas since the onset of the European Industrial Revolution. *Proceedings of the National Academy of Sciences*, *117*(8), 3967–3973.
- Gao, Y., Zhao, C., Liu, X., Zhang, M., & Leung, L. R. (2014). WRF-Chem simulations of aerosols and anthropogenic aerosol radiative forcing in East Asia. *Atmospheric Environment*, *92*, 250–266.
- Ghosh, S., Verma, S., Kuttippurath, J., & Menut, L. (2020). Wintertime radiative effects of black carbon (BC) over Indo-Gangetic Plain as modelled with new BC emission inventories in CHIMERE. *Atmospheric Chemistry and Physics Discussions*, 1–31.
- Ginoux, P., Chin, M., Tegen, I., Prospero, J. M., Holben, B., Dubovik, O., & Lin, S. J. (2001). Sources and distributions of dust aerosols simulated with the GOCART model. *Journal of Geophysical Research: Atmospheres*, *106*(D17), 20255–20273.
- Gong, P., Wang, X., Pokhrel, B., Wang, H., Liu, X., Liu, X., & Wania, F. (2019). Trans-Himalayan transport of organochlorine compounds: Three-year observations and model-based flux estimation. *Environmental Science & Technology*, *53*(12), 6773–6783.
- Grell, G. A., Dudhia, J., & Stauffer, D. R. (1994). *A description of the fifth-generation Penn State/NCAR Mesoscale Model (MM5)*.
- Grell, G. A., Peckham, S. E., Schmitz, R., McKeen, S. A., Frost, G., Skamarock, W. C., & Eder, B. (2005). Fully coupled “online” chemistry within the WRF model. *Atmospheric Environment*, *39*(37), 6957–6975.
- Guenther, A., Karl, T., Harley, P., Wiedinmyer, C., Palmer, P., & Geron, C. (2006). *Estimates of global terrestrial isoprene emissions using MEGAN (Model of Emissions of Gases and Aerosols from Nature)*.
- Gul, C., Mahapatra, P. S., Kang, S., Singh, P. K., Wu, X., He, C., et al. (2021). Black carbon concentration in the central Himalayas: Impact on glacier melt and potential source contribution. *Environmental Pollution*, *275*, 116544.
- Guo, B., Wang, Y., Zhang, X., Che, H., Ming, J., & Yi, Z. (2020). Long-term variation of black carbon aerosol in china based on revised aethalometer monitoring data. *Atmosphere*, *11*(7), 684.
- Gustafson, W. I., Chapman, E. G., Ghan, S. J., Easter, R. C., & Fast, J. D. (2007). Impact on modeled cloud characteristics due to simplified treatment of uniform cloud condensation nuclei during NEAQS 2004. *Geophysical Research Letters*, *34*(19).
- Gustafsson, Ö., & Ramanathan, V. (2016). Convergence on climate warming by black carbon aerosols. *Proceedings of the National Academy of Sciences*, *113*(16), 4243–4245.
- Han, H., Wu, Y., Liu, J., Zhao, T., Zhuang, B., Wang, H., et al. (2020). Impacts of atmospheric transport and biomass burning on the inter-annual variation in black carbon aerosols over the Tibetan Plateau. *Atmospheric Chemistry and Physics*, *20*(21), 13591–13610.
- Hansen, J., Sato, M., Ruedy, R., Lacis, A., & Oinas, V. (2000). Global warming in the twenty-first century: An alternative scenario. *Proceedings of the National Academy of Sciences*, *97*(18), 9875–9880.
- He, C., Li, Q., Liou, K. N., Takano, Y., Gu, Y., Qi, L., et al. (2014). Black carbon radiative forcing over the Tibetan Plateau. *Geophysical Research Letters*, *41*(22), 7806–7813.
- Huang, F., & Ma, W. (2016). Analysis of long-term meteorological observation for weather and climate fundamental data over the Northern Tibetan Plateau. *Advances in Meteorology*.
- Huang, X., Ding, A., Wang, Z., Ding, K., Gao, J., Chai, F., & Fu, C. (2020). Amplified transboundary transport of haze by aerosol–boundary layer interaction in China. *Nature Geoscience*, 1–7.
- Hunter, J. D. (2007). Matplotlib: A 2D graphics environment. *Computing in Science & Engineering*, *9*(3), 90–95.
- Iacono, M. J., Delamere, J. S., Mlawer, E. J., Shephard, M. W., Clough, S. A., & Collins, W. D. (2008). Radiative forcing by long-lived greenhouse gases: Calculations with the AER radiative transfer models. *Journal of Geophysical Research: Atmospheres*, *113*(D13).
- ICIMOD. (2016). Meteorological data from Yala Base Camp automatic weather station, edited, ICIMOD. <https://doi.org/10.26066/RDS.26859>
- Immerzeel, W., Petersen, L., Ragetti, S., & Pellicciotti, F. (2014). The importance of observed gradients of air temperature and precipitation for modeling runoff from a glaciated watershed in the Nepalese Himalayas. *Water Resources Research*, *50*(3), 2212–2226.
- Immerzeel, W. W., van Beek, L. P. H., & Bierkens, M. F. P. (2010). Climate change will affect the Asian water towers. *Science*, *328*(5984), 1382. <https://doi.org/10.1126/science.1183188>
- Jacobson, M. Z. (2001). Strong radiative heating due to the mixing state of black carbon in atmospheric aerosols. *Nature*, *409*(6821), 695–697.
- Janssens-Maenhout, G., Crippa, M., Guizzardi, D., Dentener, F., Muntean, M., Pouliot, G., et al. (2015). HTAP_v2. 2: A mosaic of regional and global emission grid maps for 2008 and 2010 to study hemispheric transport of air pollution. *Atmospheric Chemistry and Physics*, *15*(19), 11411–11432.

- Janssens-Maenhout, G., Dentener, F., Van Aardenne, J., Monni, S., Pagliari, V., Orlandini, L., et al. (2012). EDGAR-HTAP: A harmonized gridded air pollution emission dataset based on national inventories. *European Commission Publications Office, Ispra (Italy). JRC68434, EUR report No EUR, 25*, 299–2012.
- Ji, Z.-M. (2016). Modeling black carbon and its potential radiative effects over the Tibetan Plateau. *Advances in Climate Change Research, 7*(3), 139–144.
- Jin, L., Ganopolski, A., Chen, F., Claussen, M., & Wang, H. (2005). Impacts of snow and glaciers over Tibetan Plateau on Holocene climate change: Sensitivity experiments with a coupled model of intermediate complexity. *Geophysical Research Letters, 32*(17).
- Joshi, H., Naja, M., Singh, K., Kumar, R., Bhardwaj, P., Babu, S. S., et al. (2016). Investigations of aerosol black carbon from a semi-urban site in the Indo-Gangetic Plain region. *Atmospheric Environment, 125*, 346–359.
- Joshi, R., Liu, D., Nemitz, E., Langford, B., Mullinger, N., Squires, F., et al. (2021). Direct measurements of black carbon fluxes in central Beijing using the eddy covariance method. *Atmospheric Chemistry and Physics, 21*(1), 147–162.
- Kang, S., Xu, Y., You, Q., Flügel, W.-A., Pepin, N., & Yao, T. (2010). Review of climate and cryospheric change in the Tibetan Plateau. *Environmental Research Letters, 5*(1), 015101.
- Kang, S., Zhang, Q., Qian, Y., Ji, Z., Li, C., Cong, Z., et al. (2019). Linking atmospheric pollution to cryospheric change in the third Pole region: Current progress and future prospects. *National Science Review, 6*(4), 796–809. <https://doi.org/10.1093/nsr/nwz031>
- Kang, S., Zhang, Y., Qian, Y., & Wang, H. (2020). A review of black carbon in snow and ice and its impact on the cryosphere. *Earth-Science Reviews, 103346*.
- Karki, R., Gerlitz, L., Schickhoff, U., Scholten, T., & Böhner, J. (2017). Quantifying the added value of convection-permitting climate simulations in complex terrain: A systematic evaluation of WRF over the Himalayas. *Earth System Dynamics, 8*, 507–528.
- Kaspari, S., Painter, T. H., Gysel, M., Skiles, S., & Schwikowski, M. (2014). Seasonal and elevational variations of black carbon and dust in snow and ice in the Solu-Khumbu, Nepal and estimated radiative forcings. *Atmospheric Chemistry and Physics, 14*(15), 8089–8103.
- Kattel, D., Yao, T., Yang, K., Tian, L., Yang, G., & Joswiak, D. (2013). Temperature lapse rate in complex mountain terrain on the southern slope of the central Himalayas. *Theoretical and Applied Climatology, 113*(3–4), 671–682.
- Kopacz, M., Mauzerall, D. L., Wang, J., Leibensperger, E. M., Henze, D. K., & Singh, K. (2011). Origin and radiative forcing of black carbon transported to the Himalayas and Tibetan Plateau. *Atmospheric Chemistry and Physics, 11*(6), 2837–2852. <https://doi.org/10.5194/acp-11-2837-2011>
- Kulkarni, S., Sobhani, N., Miller-Schulze, J., Shafer, M., Schauer, J., Solomon, P., et al. (2015). Source sector and region contributions to BC and PM_{2.5} in Central Asia. *Atmospheric Chemistry and Physics, 15*(4), 1683–1705. <https://doi.org/10.5194/acp-15-1683-2015>
- Kumar, R., Barth, M., Nair, V., Pfister, G., Suresh Babu, S., Satheesh, S., et al. (2015). Sources of black carbon aerosols in South Asia and surrounding regions during the Integrated campaign for aerosols, gases and radiation Budget (ICARB). *Atmospheric Chemistry and Physics, 15*(10), 5415–5428. <https://doi.org/10.5194/acp-15-5415-2015>
- Kumar, R., Naja, M., Pfister, G., Barth, M., & Brasseur, G. (2012). Simulations over South Asia using the weather Research and forecasting model with chemistry (WRF-Chem): Set-up and meteorological evaluation. *Geoscientific Model Development, 5*(2), 321.
- Kumar, R. R., Soni, V. K., & Jain, M. K. (2020). Evaluation of spatial and temporal heterogeneity of black carbon aerosol mass concentration over India using three year measurements from IMD BC observation network. *Science of The Total Environment, 138060*.
- Li, C., Bosch, C., Kang, S., Andersson, A., Chen, P., Zhang, Q., et al. (2016). Sources of black carbon to the Himalayan–Tibetan Plateau glaciers. *Nature Communications, 7*(1), 1–7.
- Lu, Z., Streets, D. G., Zhang, Q., & Wang, S. (2012). A novel back-trajectory analysis of the origin of black carbon transported to the Himalayas and Tibetan Plateau during 1996–2010. *Geophysical Research Letters, 39*(1).
- Lu, Z., Zhang, Q., & Streets, D. G. (2011). Sulfur dioxide and primary carbonaceous aerosol emissions in China and India, 1996–2010. *Atmospheric Chemistry and Physics, 11*(18).
- Lüthi, Z., Škerlak, B., Kim, S.-W., Lauer, A., Mues, A., Rupakheti, M., & Kang, S. (2015). Atmospheric brown clouds reach the Tibetan Plateau by crossing the Himalayas. *Atmospheric Chemistry and Physics, 15*(11), 6007–6021.
- Ma, Y., Ma, W., Zhong, L., Hu, Z., Li, M., Zhu, Z., et al. (2017). Monitoring and Modeling the Tibetan Plateau's climate system and its impact on east Asia. *Scientific Reports, 7*, 44574.
- Mar, K. A., Ojha, N., Pozzer, A., & Butler, T. M. (2016). Ozone air quality simulations with WRF-Chem (v3. 5.1) over Europe: Model evaluation and chemical mechanism comparison. *Geoscientific Model Development, 9*(10).
- Marcq, S., Laj, P., Roger, J.-C., Villani, P., Sellegri, K., Bonasoni, P., et al. (2010). Aerosol optical properties and radiative forcing in the high Himalaya based on measurements at the Nepal Climate Observatory–Pyramid site (5079 m asl). *Atmospheric Chemistry and Physics, 10*(13), 5859–5872.
- Ménégoz, M., Krinner, G., Balkanski, Y., Boucher, O., Cozic, A., Lim, S., et al. (2014). Snow cover sensitivity to black carbon deposition in the Himalayas: From atmospheric and ice core measurements to regional climate simulations. *Atmospheric Chemistry and Physics, 14*(8), 4237–4249.
- Ming, J., Cachier, H., Xiao, C., Qin, D., Kang, S., Hou, S., & Xu, J. (2008). *Black carbon record based on a shallow Himalayan ice core and its climatic implications*.
- Mlawer, E. J., Taubman, S. J., Brown, P. D., Iacono, M. J., & Clough, S. A. (1997). Radiative transfer for inhomogeneous atmospheres: RRTM, a validated correlated-k model for the longwave. *Journal of Geophysical Research: Atmospheres, 102*(D14), 16663–16682.
- Mues, A., Lauer, A., Lupascu, A., Rupakheti, M., Kuik, F., & Lawrence, M. G. (2018). WRF and WRF-Chem v3. 5.1 simulations of meteorology and black carbon concentrations in the Kathmandu Valley. *Geoscientific Model Development, 11*(6).
- Nair, V. S., Solmon, F., Giorgi, F., Mariotti, L., Babu, S. S., & Moorthy, K. K. (2012). Simulation of South Asian aerosols for regional climate studies. *Journal of Geophysical Research: Atmospheres, 117*(D4).
- Nakajima, T., Yoon, S. C., Ramanathan, V., Shi, G. Y., Takemura, T., Higurashi, A., et al. (2007). Overview of the atmospheric Brown cloud east Asian regional experiment 2005 and a study of the aerosol direct radiative forcing in East Asia. *Journal of Geophysical Research: Atmospheres, 112*(D24).
- Norris, J., Carvalho, L. M., Jones, C., & Cannon, F. (2020). Warming and drying over the central Himalaya caused by an amplification of local mountain circulation. *Climate and Atmospheric Science, 3*(1), 1–11.
- Pan, X., Chin, M., Gautam, R., Bian, H., Kim, D., Colarco, P. R., et al. (2015). *A multi-model evaluation of aerosols over South Asia: Common problems and possible causes*.
- Paulson, C. A. (1970). The mathematical representation of wind speed and temperature profiles in the unstable atmospheric surface layer. *Journal of Applied Meteorology, 9*(6), 857–861.
- Pokharel, M., Guang, J., Liu, B., Kang, S., Ma, Y., Holben, B. N., et al. (2019). Aerosol properties over Tibetan Plateau from a decade of AERONET measurements: Baseline, types, and influencing factors. *Journal of Geophysical Research: Atmospheres, 124*(23), 13357–13374.

- Rai, M., Mahapatra, P. S., Gul, C., Kayastha, R. B., Panday, A. K., & Puppala, S. P. (2019). Aerosol radiative forcing estimation over a remote high-altitude location (~4900 masl) near Yala Glacier, Nepal. *Aerosol and Air Quality Research*, 19(8), 1872–1897.
- Raju, A., Parekh, A., Chowdary, J., & Gnanaseelan, C. (2015). Assessment of the Indian summer monsoon in the WRF regional climate model. *Climate Dynamics*, 44(11–12), 3077–3100.
- Ramachandran, S., Rupakheti, M., & Lawrence, M. G. (2020). Black carbon dominates the aerosol absorption over the Indo-Gangetic Plain and the Himalayan foothills. *Environment International*, 142, 105814.
- Ramanathan, V., & Carmichael, G. (2008). Global and regional climate changes due to black carbon. *Nature Geoscience*, 1(4), 221–227.
- Rana, S., McGregor, J., & Renwick, J. (2015). Precipitation seasonality over the Indian subcontinent: An evaluation of gauge, reanalyses, and satellite retrievals. *Journal of Hydrometeorology*, 16(2), 631–651.
- Ravishankara, A., David, L. M., Pierce, J. R., & Venkataraman, C. (2020). Outdoor air pollution in India is not only an urban problem. *Proceedings of the National Academy of Sciences*, 117(46), 28640–28644.
- Sarangi, C. N., Qian, Y., Rittger, K., Bormann, K. J., Liu, Y., Wang, H., et al. (2019). Impact of light-absorbing particles on snow albedo darkening and associated radiative forcing over high-mountain Asia: High-resolution WRF-Chem modeling and new satellite observations. *Atmospheric Chemistry and Physics*, 19. PNNL-SA-146241.
- Shah, H. L., & Mishra, V. (2016). Uncertainty and bias in satellite-based precipitation estimates over Indian subcontinental basins: Implications for real-time streamflow simulation and flood prediction. *Journal of Hydrometeorology*, 17(2), 615–636.
- Singh, P., Sarawade, P., & Adhikary, B. (2020). Transport of black carbon from planetary boundary layer to free troposphere during the summer monsoon over South Asia. *Atmospheric Research*, 235, 104761.
- Skamarock, W. C., Klemp, J., Dudhia, J., Gill, D., Barker, D., Wang, W., & Powers, J. (2005). A description of the Advanced Research WRF version 2. NCAR Tech. *Forecasting Report*. Note NCAR/TN-4681STR.
- Slater, J., Coe, H., McFiggans, G., Tontila, J., & Romakkaniemi, S. (2021). The effect of black carbon on aerosol-boundary layer feedback: Potential implications for Beijing haze episodes. *Atmospheric Chemistry and Physics Discussions*, 2021, 1–23. <https://doi.org/10.5194/acp-2021-139>
- Song, Y., Chen, G., & Wang, W.-C. (2019). Aerosol direct radiative and cloud adjustment effects on Surface climate over eastern China: Analyses of WRF Model Simulations. *Journal of Climate*, 32(4), 1293–1306.
- Stull, R. B. (1988). *An introduction to boundary layer meteorology*. Springer Science & Business Media.
- Sun, Q., Miao, C., Duan, Q., Ashouri, H., Sorooshian, S., & Hsu, K. L. (2018). A review of global precipitation data sets: Data sources, estimation, and intercomparisons. *Reviews of Geophysics*, 56(1), 79–107.
- Ueno, K., Toyotsu, K., Bertolani, L., & Tartari, G. (2008). Stepwise onset of monsoon weather observed in the Nepal Himalaya. *Monthly Weather Review*, 136(7), 2507–2522.
- Ukhov, A., Mostamandi, S., da Silva, A., Flemming, J., Alshehri, Y. M., Shevchenko, I., & Stenichkov, G. L. (2020). *Assessment of natural and anthropogenic aerosol air pollution in the Middle East using MERRA-2, CAMS data assimilation products, and high-resolution WRF-Chem model simulations*.
- Viviroli, D., Dürr, H. H., Messerli, B., Meybeck, M., & Weingartner, R. (2007). Mountains of the world, water towers for humanity: Typology, mapping, and global significance. *Water resources research*, 43(7).
- Wang, Z., Huang, X., & Ding, A. (2018). Dome effect of black carbon and its key influencing factors: A one-dimensional modelling study. *Atmospheric Chemistry and Physics*, 18(4), 2821–2834. <https://doi.org/10.5194/acp-18-2821-2018>
- Weedon, G. P., Balsamo, G., Bellouin, N., Gomes, S., Best, M. J., & Viterbo, P. (2014). The WFDEI meteorological forcing data set: WATCH forcing data methodology applied to ERA-interim reanalysis data. *Water Resources Research*, 50(9), 7505–7514.
- Whiteman, C. D. (2000). *Mountain meteorology: Fundamentals and applications*. Oxford University Press.
- Wiedinmyer, C., Akagi, S., Yokelson, R. J., Emmons, L., Al-Saadi, J., Orlando, J., & Soja, A. (2011). The fire INventory from NCAR (FINN): A high resolution global model to estimate the emissions from open burning. *Geoscientific Model Development*, 4(3), 625.
- Wiscombe, W., & Grams, G. (1976). The backscattered fraction in two-stream approximations. *Journal of the Atmospheric Sciences*, 33(12), 2440–2451.
- Xu, R., Tie, X., Li, G., Zhao, S., Cao, J., Feng, T., & Long, X. (2018). Effect of biomass burning on black carbon (BC) in South Asia and Tibetan Plateau: The analysis of WRF-Chem modeling. *The Science of the Total Environment*, 645, 901–912.
- Xu, X., Zhao, T., Lu, C., Guo, Y., Chen, B., Liu, R., et al. (2014). An important mechanism sustaining the atmospheric "water tower" over the Tibetan Plateau. *Atmospheric Chemistry and Physics*, 14(20), 11287–11295.
- Xu, Y., Ramanathan, V., & Washington, W. (2016). Observed high-altitude warming and snow cover retreat over Tibet and the Himalayas enhanced by black carbon aerosols. *Atmospheric Chemistry and Physics*, 16(3), 1303–1315. <https://doi.org/10.5194/acp-16-1303-2016>
- Yang, J., Kang, S., Ji, Z., & Chen, D. (2018). Modeling the origin of anthropogenic black carbon and its climatic effect over the Tibetan Plateau and surrounding regions. *Journal of Geophysical Research: Atmospheres*, 123(2), 671–692.
- Yao, T., Xue, Y., Chen, D., Chen, F., Thompson, L., Cui, P., et al. (2019). Recent third pole's rapid warming accompanies cryospheric melt and water cycle intensification and interactions between monsoon and environment: Multidisciplinary approach with observations, modeling, and analysis. *Bulletin of the American Meteorological Society*, 100(3), 423–444.
- You, H., Kun, Y., Tandong, Y., & Jie, H. (2012). Numerical simulation of a heavy precipitation in Qinghai-Xizang Plateau based on WRF model. *Plateau Meteor*, 31(5), 1183–1191.
- You, Q., Chen, D., Wu, F., Pepin, N., Cai, Z., Ahrens, B., et al. (2020). Elevation dependent warming over the Tibetan Plateau: Patterns, mechanisms and perspectives. *Earth-Science Reviews*, 103349.
- You, Q., Fraedrich, K., Ren, G., Pepin, N., & Kang, S. (2013). Variability of temperature in the Tibetan Plateau based on homogenized surface stations and reanalysis data. *International Journal of Climatology*, 33(6), 1337–1347.
- Yuan, Q., Wan, X., Cong, Z., Li, M., Liu, L., Shu, S., et al. (2020). In Situ observations of light-absorbing carbonaceous aerosols at Himalaya: Analysis of the South Asian Sources and trans-Himalayan valleys transport pathways. *Journal of Geophysical Research: Atmospheres*, 125(18), e2020JD032615.
- Yuan, R., Zhang, X., Liu, H., Gui, Y., Shao, B., Tao, X., et al. (2019). Aerosol vertical mass flux measurements during heavy aerosol pollution episodes at a rural site and an urban site in the Beijing area of the North China Plain. *Atmospheric Chemistry and Physics*, 19(20), 12857–12874.
- Yuan, T., Chen, S., Wang, L., Yang, Y., Bi, H., Zhang, X., & Zhang, Y. (2020). Impacts of two east Asian atmospheric circulation Modes on black carbon aerosol over the Tibetan Plateau in winter. *Journal of Geophysical Research: Atmospheres*, 125(12), e2020JD032458. <https://doi.org/10.1029/2020JD032458>

- Yuan, X., Ji, P., Wang, L., Liang, X. Z., Yang, K., Ye, A., et al. (2018). High-resolution land Surface Modeling of hydrological changes over the Sanjiangyuan region in the eastern Tibetan Plateau: 1. Model development and evaluation. *Journal of Advances in Modeling Earth Systems*, *10*(11), 2806–2828.
- Zaveri, R. A., Easter, R. C., Fast, J. D., & Peters, L. K. (2008). Model for simulating aerosol interactions and chemistry (MOSAIC). *Journal of Geophysical Research: Atmospheres*, *113*(D13).
- Zaveri, R. A., & Peters, L. K. (1999). A new lumped structure photochemical mechanism for large-scale applications. *Journal of Geophysical Research: Atmospheres*, *104*(D23), 30387–30415. <https://doi.org/10.1029/1999JD900876>
- Zeb, B., Alam, K., Nasir, J., Mansha, M., Ahmad, I., Bibi, S., et al. (2020). Black Carbon aerosol characteristics and radiative forcing over the high altitude glacier region of Himalaya-Karakorum-Hindukush. *Atmospheric Environment*, 117711.
- Zhang, M., Zhao, C., Cong, Z., Du, Q., Xu, M., Chen, Y., et al. (2020). Impact of topography on black carbon transport to the southern Tibetan Plateau during the pre-monsoon season and its climatic implication. *Atmospheric Chemistry and Physics*, *20*(10).
- Zhang, R., Wang, H., Qian, Y., Rasch, P. J., Easter, R. C., Ma, P.-L., et al. (2015). Quantifying sources, transport, deposition and radiative forcing of black carbon over the Himalayas and Tibetan Plateau. *Atmospheric Chemistry and Physics Discussions*, *15*(11), 6205–6223. <https://doi.org/10.5194/acp-15-6205-2015>
- Zhang, R., Wang, Y., He, Q., Chen, L., Zhang, Y., Qu, H., et al. (2017). Enhanced trans-Himalaya pollution transport to the Tibetan Plateau by cut-off low systems. *Atmospheric Chemistry and Physics*, *17*(4), 3083–3095.
- Zhang, X., Chen, S., Kang, L., Yuan, T., Luo, Y., Alam, K., et al. (2020). Direct radiative forcing induced by light-absorbing aerosols in different climate regions over East Asia. *Journal of Geophysical Research: Atmospheres*, *125*(14), e2019JD032228.
- Zhang, Y., Sartelet, K., Zhu, S., Wang, W., Wu, S.-Y., Zhang, X., et al. (2013). Application of WRF/Chem-MADRID and WRF/Polyphemus in Europe-Part 2: Evaluation of chemical concentrations and sensitivity simulations. *Atmospheric Chemistry and Physics*, *13*(14).
- Zhang, Y., Zhang, X., Wang, L., Zhang, Q., Duan, F., & He, K. (2016). Application of WRF/Chem over east Asia: Part I. Model evaluation and intercomparison with MM5/CMAQ. *Atmospheric Environment*, *124*, 285–300.
- Zhao, C., Chen, S., Leung, L. R., Qian, Y., Kok, J. F., Zaveri, R. A., & Huang, J. (2013). Uncertainty in modeling dust mass balance and radiative forcing from size parameterization. *Atmospheric Chemistry and Physics*, *13*(21), 10733–10753. <https://doi.org/10.5194/acp-13-10733-2013>
- Zhao, C., Hu, Z., Qian, Y., Ruby Leung, L., Huang, J., Huang, M., et al. (2014). Simulating black carbon and dust and their radiative forcing in seasonal snow: A case study over north China with field campaign measurements. *Atmospheric Chemistry and Physics*, *14*(20), 11475–11491.
- Zhao, C., Liu, X., Leung, L., Johnson, B., McFarlane, S. A., Gustafson, W., Jr, et al. (2010). The spatial distribution of mineral dust and its shortwave radiative forcing over north Africa: Modeling sensitivities to dust emissions and aerosol size treatments. *Atmospheric Chemistry and Physics*, *10*(18), 8821.
- Zhao, M., Dai, T., Wang, H., Bao, Q., Liu, Y., & Shi, G. (2021). Modelling study on the source contribution to aerosol over the Tibetan Plateau. *International Journal of Climatology*, *41*(5), 3247–3265.
- Zhao, S., Tie, X., Long, X., & Cao, J. (2017). Impacts of Himalayas on black carbon over the Tibetan Plateau during summer monsoon. *The Science of the Total Environment*, *598*, 307–318.
- Zhao, S., Yin, D., Yu, Y., Kang, S., Qin, D., & Dong, L. (2020). *PM2.5 and O3 pollution during 2015–2019 over 367 Chinese cities: Spatiotemporal variations, meteorological and topographical impacts*. Environmental Pollution.
- Zhao, T., & Yatagai, A. (2014). Evaluation of TRMM 3B42 product using a new gauge-based analysis of daily precipitation over China. *International Journal of Climatology*, *34*(8), 2749–2762.
- Zhu, X., Wang, W., & Fraedrich, K. (2013). Future climate in the Tibetan Plateau from a statistical regional climate model. *Journal of Climate*, *26*(24), 10125–10138.